



Contents lists available at ScienceDirect

Electrochimica Acta

journal homepage: [www.elsevier.com/locate/electacta](http://www.elsevier.com/locate/electacta)

## Corrosion modelling of iron based alloy in nuclear waste repository

C. Bataillon<sup>a,\*</sup>, F. Bouchon<sup>b,c</sup>, C. Chainais-Hillairet<sup>b,c</sup>, C. Desgranges<sup>a</sup>, E. Hoarau<sup>e</sup>,  
F. Martin<sup>a</sup>, S. Perrin<sup>a</sup>, M. Tupin<sup>d</sup>, J. Talandier<sup>e</sup>

<sup>a</sup> CEA, DEN, DPC, SCCME, F-91191 Gif sur Yvette, France

<sup>b</sup> Clermont Université, Université Blaise Pascal, Laboratoire de Mathématiques, BP10448, F-63000 Clermont-Ferrand, France

<sup>c</sup> CNRS, UMR 6620, Laboratoire de Mathématiques, F-63177 Aubière, France

<sup>d</sup> CEA, DEN, DMN, SEMI, LM2E, F-91191 Gif sur Yvette, France

<sup>e</sup> ANDRA/DS, 92298 Châtenay-Malabry Cedex, France

### ARTICLE INFO

#### Article history:

Received 14 October 2009

Received in revised form 25 February 2010

Accepted 27 February 2010

Available online xxx

#### Keywords:

PDM

Poisson

Oxide layer

Iron

Mott–Schottky

### ABSTRACT

The Diffusion Poisson Coupled Model (DPCM) is presented to modelling the oxidation of a metal covered by an oxide layer. This model is similar to the Point Defect Model and the Mixed Conduction Model except for the potential profile which is not assumed but calculated in solving the Poisson equation. This modelling considers the motions of two moving interfaces linked through the ratio of Pilling–Bedworth. Their locations are unknowns of the model. Application to the case of iron in neutral or slightly basic solution is discussed. Then, DPCM has been first tested in a simplified situation where the locations of interfaces were fixed. In such a situation, DPCM is in agreement with Mott–Schottky model when iron concentration profile is homogeneous. When it is not homogeneous, deviation from Mott–Schottky model has been observed and is discussed. The influence of the outer and inner interfacial structures on the kinetics of electrochemical reactions is illustrated and discussed. Finally, simulations for the oxide layer growth are presented. The expected trends have been obtained. The steady-state thickness is a linear function of the applied potential and the steady-state current density is potential independent.

© 2010 Elsevier Ltd. All rights reserved.

### 1. Introduction

The long-term behaviour of nuclear waste canisters in geological repository depends on (i) Thermo-Hydro-Mechanical (THM) behaviour of ground soils, (ii) metallic materials used to manufacture canisters and (iii) geochemical features of the ground in contact with the canisters. The disposal of nuclear waste canisters must be considered as a disturbance of the state of the clay fossil soil because (i) the canister is a source of heat but also because (ii) metallic canister corrodes. In clay soil, corrosion products like hydrogen and/or metallic cations induce geochemical transformations of the clay which induce changes in pH and redox potential of the surrounding clay of canisters which induce changes in corrosion conditions. In other words, the corrosion process and the geochemical transformations are linked. The 1000-years behaviour of metallic nuclear waste canisters could be predicted in linking corrosion, geochemical and THM models. The purpose of this paper is to propose an electrochemical model for this target.

This task seemed quite easy since at least two models have been proposed in the literature, i.e. the Point Defect Model

[1–11] and the Mixed Conduction Model [12–16]. Both models assume that the metal is covered by a dense oxide layer. Mass and charges transports through the oxide layer are described as a field assisted diffusion of ionic defects or species. The PDM uses the Nernst–Planck equation whereas the MCM uses the Fromhold–Cook equation. Both models assume that the field strength in the layer is homogeneous and independent of the potential ( $V = E - E_{SHE}$ ). The whole voltage drop  $V$  is distributed as two interfacial drops ( $\Delta\phi_{m/f}$ ,  $\Delta\phi_{f/s}$ ) and a bulk voltage  $\varepsilon L$ :

$$V = \Delta\phi_{m/f} + \varepsilon L + \Delta\phi_{f/s} \quad (1)$$

where  $\varepsilon$  is the homogeneous field and  $L$  the layer thickness. To be consistent, both models introduce a parameter  $\alpha_{f/s}$  called the outer interface polarizability which is defined as:

$$\Delta\phi_{f/s} = \alpha_{f/s} V + \Delta\phi_{f/s}^0 \quad (2)$$

where  $\alpha_{f/s}$  is constant and  $\Delta\phi_{f/s}^0$  is a function of the external oxidizing conditions. For instance,  $\Delta\phi_{f/s}^0$  is a linear function of pH [1]. In the case of the PDM,  $\varepsilon$  and  $\alpha_{f/s}$  for iron have been estimated from the variation of the thickness  $L$  vs. potential  $E$  in borate buffer [1,17,18]. In the case of the MCM,  $\varepsilon$  and  $\alpha_{f/s}$  have been estimated from Contact Electrical Impedance spectra [13].

Unfortunately, the fact that  $\varepsilon$  and  $\alpha_{f/s}$  are free adjustable constant parameters implies that the application of the model could be

\* Corresponding author. Tel.: +33 01 69 08 15 91; fax: +33 01 69 08 15 86.  
E-mail address: [christian.bataillon@cea.fr](mailto:christian.bataillon@cea.fr) (C. Bataillon).

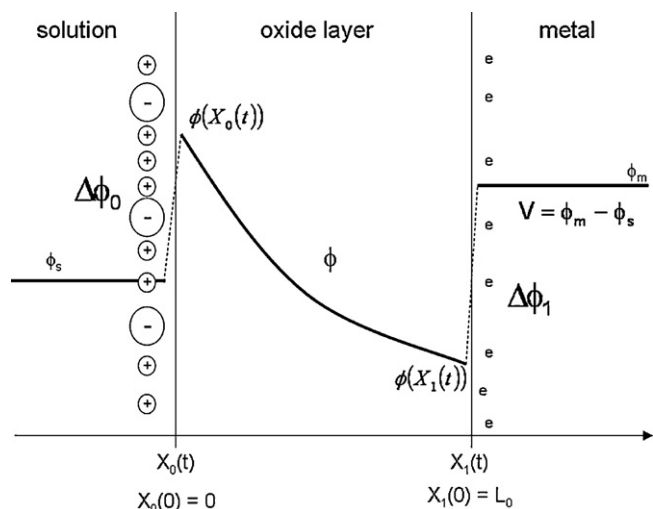


Fig. 1. Potential profile in the solution/oxide layer/metal system.

restricted to some bounded range of oxidizing conditions expressed in terms of potential range and chemical composition of the oxidizing solution. This is a paramount problem to link the corrosion model with other models which will describe the evolution of the oxidizing conditions. From a scientific point of view,  $\varepsilon$  and  $\alpha_{f/s}$  have been introduced to describe the potential profile in the solution-oxide layer–metal system. This profile is basically the solution of the Poisson equation. The aim of this paper is to propose a model which takes explicitly into account the Poisson equation. This task is not so simple because the numerical resolution of the coupled Poisson and Fick equations is not trivial. Recently, Vankerberghen [19] has proposed a numerical resolution based on a finite-elements method. This resolution has been carried out with very special parameter values which lead to symmetric concentration profiles. Moreover, the net electroneutrality was restricted to the oxide layer which will lead to a symmetric field profile.

## 2. The basic equations of the modelling

Solid state transport of charge carriers in compact oxide layer is considered. These charge carriers could be point defects [20] or ions, electrons or holes. The whole system consists in a solution in contact with an oxide layer which covers a metal. Two interfaces bound the oxide layer. One is the inner interface which corresponds to the metal/oxide one. The other is the outer interface which corresponds to the oxide/solution interface. The metal is an electronic conductor. It could be charged either by accumulation or depletion of electrons. The solution is an ionic conductor. It could be charged either by accumulation of cations or anions. The oxide layer is a mixed electronic and ionic conductor (see Fig. 1).

Neither combination nor creation of charge carriers is considered inside the oxide layer. The charge carriers are created at one interface (inner or outer) and are consumed at the other (outer or inner). Inside the oxide layer, each charge carrier flux is assumed independent of the others because the physical mechanism for transport is generally typical of the kind of charge carrier (electronic transport in a conduction band, transport of ions by a vacancy mechanism, etc.).

### 2.1. The potential profile equations

The potential profile  $\phi$  is given by the Poisson equation:

$$\nabla^2 \phi = -\frac{F}{\chi \chi_0} \sum_i z_i c_i - \frac{\rho_{hl}}{\chi \chi_0} \quad (3)$$

where  $\nabla^2$  is the Laplacian.  $\chi$  is the dielectric constant of the oxide,  $\chi_0$  the vacuum dielectric constant and  $F$  the Faraday constant.  $c_i$  is the concentration profile of the charge carrier  $i$  inside the layer,  $z_i$  its charge. The first term in the right hand side of (3) corresponds to the charge carriers. The second term  $\rho_{hl}$  corresponds to the net charge density of the host lattice (see Section 3.1.2). It has been assumed homogeneous.

As mentioned above, the solution and the metal could be charged. The charge of the solution  $\sigma_0$  generates a field in the oxide layer. The same argument stands for the charge  $\sigma_1$  carried by the metal. As a consequence, the interfacial charges generate a local field in the oxide layer in the vicinity of the corresponding interface (outer and inner). These local fields are given by Gauss laws:

$$\begin{cases} \text{grad } \phi[X_0(t)] = -\frac{\sigma_0[\Delta\phi_0]}{\chi \chi_0} \\ \text{grad } \phi[X_1(t)] = +\frac{\sigma_1[\Delta\phi_1]}{\chi \chi_0} \end{cases} \quad (4)$$

where  $\Delta\phi_0$  and  $\Delta\phi_1$  are respectively the voltage drop at the outer and the inner interfaces (see Fig. 1). Taking the potential of the solution  $\phi_s$  as reference, the two boundary conditions are given by:

$$\begin{cases} \phi(X_0(t)) = \Delta\phi_0 \\ \phi(X_1(t)) = V - \Delta\phi_1 \end{cases} \quad (5)$$

where  $V$  is the applied potential between the metal and the solution (see Fig. 1).

It has been assumed that the interfacial charges of the solution  $\sigma_0$  and of the metal  $\sigma_1$  are described by:

$$\begin{cases} \sigma_0[\Delta\phi_0] = -\int_{\Delta\phi_1^{pzc}}^{\Delta\phi_0} \Gamma_0[\xi] d\xi \\ \sigma_1[\Delta\phi_1] = \int_{\Delta\phi_1^{pzc}}^{\Delta\phi_1} \Gamma_1[\xi] d\xi \end{cases} \quad (6)$$

The interfacial structure (outer and inner) has been described by a differential capacitance ( $\Gamma_0$  and  $\Gamma_1$ ) and a corresponding voltage of zero charge ( $\Delta\phi_0^{pzc}$  and  $\Delta\phi_1^{pzc}$ ).

In the Diffusion Poisson Coupled Model (DPCM), the first integration of the Poisson equation (3) over the whole layer (from  $X_0(t)$  to  $X_1(t)$ , see Fig. 1) gives:

$$\begin{aligned} \text{grad } \phi[X_1(t)] - \text{grad } \phi[X_0(t)] \\ = -\frac{F}{\chi \chi_0} \sum_i z_i \int_{X_0(t)}^{X_1(t)} c_i[x] dx - \frac{\rho_{hl}}{\chi \chi_0} (X_1(t) - X_0(t)) \end{aligned} \quad (7)$$

Introducing the Gauss laws (4), the net electroneutrality equation is obtained:

$$\sigma_0[\Delta\phi_0] + F \sum_i z_i \int_{X_0(t)}^{X_1(t)} c_i[x] dx + \rho_{hl}(X_1(t) - X_0(t)) + \sigma_1[\Delta\phi_1] = 0 \quad (8)$$

In the simplest case where the oxide layer does not contain any charge carrier ( $c_i \equiv 0$ ) and is stoichiometric ( $\rho_{hl} = 0$ ), the net electroneutrality of the whole system implies that  $\sigma_0 = -\sigma_1$ . So, the two local fields defined by (4) are equal. This limiting case corresponds to those of a pure capacitance.

### 2.2. The moving boundaries equations

It has been assumed that the outer and the inner interfaces could move with time. The origin of the space axis is the location of the outer interface  $X_0(0)$  at the initial time ( $t = 0$ ). The initial thickness  $L_0$  of the oxide layer defines the initial location of the inner interface  $X_1(0) = L_0$  (see Fig. 1).

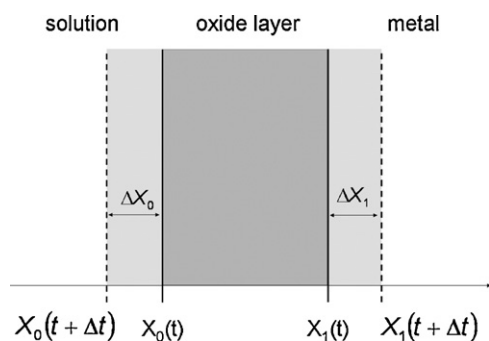


Fig. 2. Evolution of the oxide thickness due to the oxidation of the metal by the oxide growth step.

Let us consider a step which consumes the metal to produce the oxide host lattice (OHL). Then, the inner interface moves toward the positive direction as depicted in Fig. 2. Let us call this shift  $\Delta X_1$ . It corresponds to the oxidation of  $\Delta X_1 S / \Omega_M$  mole of metal; where  $\Omega_M$  is the molar volume of the metal and  $S$  the sample surface. Assuming that the oxide contains  $m$  metal cations per mole of oxide ( $m=3$  for magnetite),  $\Delta X_1 S / m \Omega_M$  mole of OHL are built. It corresponds to an increase of the layer thickness  $\Delta L = \Delta X_1 - \Delta X_0$  as depicted in Fig. 2. The number of mole of OHL is also equal to  $\Delta L S / \Omega_{ox}$ . Then, from the mass balance:

$$\Delta X_0 = \Delta X_1 \left( 1 - \frac{\Omega_{ox}}{m \Omega_M} \right) \quad (9)$$

This relation shows that the shift of the inner interface is linked to a shift of the outer interface through the ratio of Pilling–Bedworth  $\Omega_{ox} / m \Omega_M$ . When this ratio is greater than one and assuming that the outer interface can move freely, the shift of the inner interface toward the positive direction is linked to a shift of the outer interface toward the negative direction as depicted in Fig. 2. If the outer interface cannot move freely then compressive stresses will be induced in the oxide layer.

At the outer interface, the OHL is in close contact with the solution. It could be dissolved in the solution at a net rate called  $v_d(t)$ . The mathematical expression of  $v_d(t)$  will depend on the mechanism to describe this step. The net shift of the outer interface will be the sum of two contributions; one coming from the dissolution step and the other coming from the inner OHL growth step:

$$\frac{dX_0}{dt} = v_d(t) + \frac{dX_1}{dt} \left( 1 - \frac{\Omega_{ox}}{m \Omega_M} \right) \quad (10)$$

The second term has been obtained in deriving (9) vs. time. Once more, the mathematical expression for  $dX_1/dt$  will depend on the mechanism considered for the OHL growth step.

### 2.3. The transport equations

It has been assumed for now that the flux is given by the Nernst–Planck equation:

$$J_i = -D_i \text{grad } c_i - z_i \gamma D_i c_i \text{grad } \phi \quad (11)$$

where  $D_i$  is the diffusion coefficient of the charge carrier  $i$  and  $\gamma = F/RT$ . This implies that the field inside the oxide layer is not too high. Otherwise, The Fromhold–Cook equation must be considered [12]. The second generalized Fick equation gives the time variation of the concentration profile:

$$\frac{\partial c_i}{\partial t} = -\text{div } J_i \quad (12)$$

To integrate this partial differential equation, two concentrations called  $c_i^0$  and  $c_i^1$  are needed.  $c_i^0$  and  $c_i^1$  are respectively the outer and

the inner interfacial charge carrier concentrations. These concentrations are the solutions of the flux balance equations which state that the net outer and inner interfacial reaction rates are equal to the corresponding flux  $J_i$ . The mathematical expressions of these interfacial reactions rates depend on the mechanism considered to describe the mass and electron exchanges at the outer and the inner interfaces. There are specific of the case under consideration. This point is treated below for the case of iron is neutral solution.

### 3. Oxidation of iron in neutral or slightly basic solution

It has been shown [21,22] that in anaerobic saturated clay, the solution inside the porosity of the clay is nearly neutral or slightly alkaline ( $7 < \text{pH} < 8$ ). Then, iron would be covered with a spinel iron oxide layer ( $\text{Fe}_{3-\delta}\text{O}_4$ ) intermediate between magnetite ( $\delta = 0$ ) and maghemite ( $\delta = 1/3$ ).

#### 3.1. Identification of charge carriers

##### 3.1.1. The electronic charge carrier

Electronic conduction of magnetite has been extensively studied since 90 years [23]. Nowadays, the most advanced modelling has been proposed by Ihle and Lorenz [24]. This model seems to drop the usual description of magnetite which invokes both ferrous and ferric cations  $[\text{Fe}_T^{+II}\text{Fe}_O^{+III}\text{Fe}_O^{+III}\text{O}_4]$ . This view is confirmed by electronic conductivity measurements [25], showing that the electronic conductivity over a large range of temperatures for  $\text{NiFe}_2\text{O}_4$  is 10 orders of magnitude lower than to the one obtained for magnetite. This difference shows that the high electronic conductivity of magnetite is inconsistent with the existence of divalent cations as in  $\text{NiFe}_2\text{O}_4$ . This view is also supported by Mossbauer spectroscopy. For the low temperature phase ( $T=78$  K below Verwey transition), Iida et al. [26] could observed lines associated with  $\text{Fe}^{+III}$  and  $\text{Fe}^{+II}$  in octahedral position. On the contrary, Coey et al. [27] claim that separate lines for  $\text{Fe}^{+III}$  and  $\text{Fe}^{+II}$  are not observed for magnetite at room temperature because the characteristic time for electron interchange is so high thus the nucleus experiences an average electronic configuration between  $\text{Fe}^{+II}$  and  $\text{Fe}^{+III}$ . In this paper, electron in band conduction has been assumed because room temperature is concerned.

##### 3.1.2. The cationic charge carrier

An extensive study of cations diffusion in magnetite has been published by Dieckmann et al. [28–34]. Radiotracer technique has been used on synthetic non-stoichiometric magnetite ( $-0.005 < \delta < 0.09$ ) in temperature ranging from 900 to 1400 °C. It has been shown that for the lowest temperatures, cationic diffusion is completely due to octahedral iron cations. Tetrahedral iron cations are static. The cations diffusion proceeds by a vacancy mechanism [28,29] for  $\delta > 0$  and by interstitial mechanism for  $\delta < 0$ . On the other hand, Davenport et al. [35] have studied by X-ray diffraction, with a synchrotron, the structure of the passive layer formed electrochemically on iron in borate buffer. They claimed that the major feature of the oxide layer stands in the different occupancies of tetrahedral and octahedral sites compared to those of the magnetite. Only 80% of octahedral sites and 66% of tetrahedral sites were occupied. There were about 12% of the so-called *octahedral interstitial* cations.

The well ordered magnetite studied by Dieckmann would be depicted by  $[2\text{Fe}_O^{+III}\text{Fe}_T^{+III}\text{O}_4] \cdot (\delta V_{\text{Fe}_O}^{3\bullet}, ne)$  for sub-stoichiometric domain ( $\delta > 0$ ) and by  $[2\text{Fe}_O^{+III}\text{Fe}_T^{+III}\text{O}_4] \cdot (|\delta| \text{Fe}_O^{\bullet\bullet}, ne)$  for the over stoichiometric domain ( $\delta < 0$ ). The aim of this notation is to outline which moves in what. The static host lattice is depicted inside the brackets, whereas the moving charge carriers are listed inside parenthesis. On the contrary, the oxide film analyzed by Davenport could be depicted by  $[\text{Fe}_T^{+III}\text{O}_4]^{5\bullet} \cdot ((2-\delta)\text{Fe}_O^{\bullet\bullet}, ne)$ . One can con-

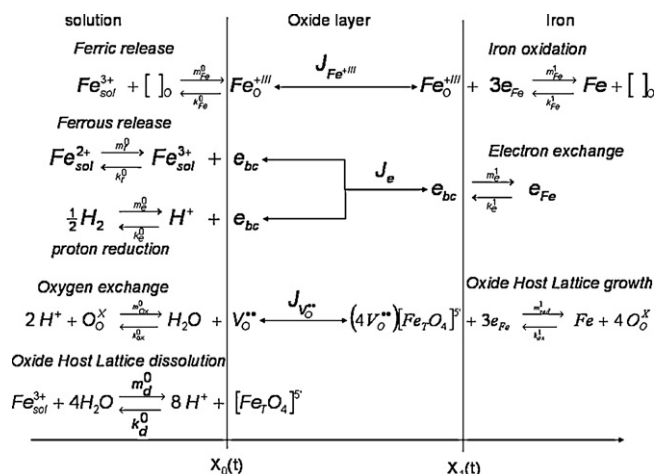


Fig. 3. Flow chart for electrons, octahedral cations and oxygen vacancies. Kröger–Vink notation is used. [ ]<sub>o</sub> corresponds to a free octahedral site.

sider in first approximation that moving cations could occupy any octahedral site. It must be noticed that this description could be extended over the whole stoichiometric domain ( $-0.005 < \delta < 1/3$ ). In this case, the cations diffusion proceeds neither by vacancy nor interstitial mechanism but rather by a hopping mechanism because the numbers of empty or occupied octahedral sites are of the same order of magnitude.

### 3.2. The interfacial reactions

The interfacial reaction path depends on the kind of charge carriers involved in the transport through the OHL. In the framework of this paper, octahedral iron cations, electrons and oxygen vacancies are considered. The flow chart depicted in Fig. 3 is proposed.

#### 3.2.1. Iron oxidation

Octahedral iron cations are created at the inner interface by the ( $k_{Fe}^1$ ) direction of the iron oxidation step. The net flux of octahedral cations is:

$$J_{Fe^III}(X_1) = m_{Fe}^1 c_{Fe}^1 \exp(-3b_{Fe}^1 \gamma(V - \phi(X_1))) - k_{Fe}^1 (c_{Fe}^m - c_{Fe}^1) \exp(3a_{Fe}^1 \gamma(V - \phi(X_1))) \quad (13)$$

where  $c_{Fe}^m$  is the maximum occupancy for octahedral iron cations in the OHL. It corresponds to the phase transformation of magnetite in sub-stoichiometric wustite. From the Thermo-Calc database, this maximum occupancy is independent of the temperature around room temperature and is equal to  $c_{Fe}^m = 2.005/\Omega_{ox}$ .

The transfer of an iron atom from the steel to the OHL lets a vacancy in the steel. In the opposite direction, the transfer of a ferric cation from the OHL to the steel needs to consume a vacancy in the steel. It has been assumed that the concentration of metal vacancies is constant and monitored by the micro-structure of the steel. So, the concentration of metal vacancies does not appear in (13). It is integrated in the kinetic constants which depend on the micro-structure of the steel.

#### 3.2.2. Ferric release

Octahedral iron cations are consumed at the outer interface by the ( $k_{Fe}^0$ ) direction of the ferric release step. The net flux of octahedral cations is:

$$J_{Fe^III}(X_0) = m_{Fe}^0 a_{Fe^{3+}} (c_{Fe}^m - c_{Fe}^0) \exp(-3b_{Fe}^0 \gamma \phi(X_0)) - k_{Fe}^0 c_{Fe}^0 \exp(3a_{Fe}^0 \gamma \phi(X_0)) \quad (14)$$

where  $a_{Fe^{3+}}$  is activity of  $Fe^{3+}$  in solution.

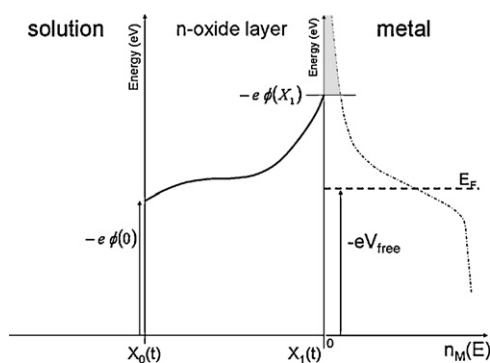


Fig. 4. Band diagram for the contact between the solution-oxide layer–metal at thermal equilibrium.  $n_M(E)$  is the concentration of electrons in the metal.

#### 3.2.3. Electronic exchange

Electrons are exchanged at the inner interface between the conduction bands of the iron and the OHL. It has been assumed that this exchange is described by the thermo-electronic emission rule [36]. No tunnelling is considered here. It implies that the thickness of the oxide layer is greater than 1 or 2 nm. The net flux of electrons at the inner interface is given by:

$$J_e(X_1) = m_e^1 c_e^1 - k_e^1 c_e^{metal} \quad (15)$$

where  $c_e^{metal}$  depends on the band diagram for the metal-oxide contact. Such a band diagram is depicted in Fig. 4.  $c_e^{metal}$  corresponds to the gray part at the left of the density of electrons in the metal  $n_M(E)$ :

$$c_e^{metal} = \int_{-e\phi(X_1)}^{+\infty} \frac{g(E)}{1 + \exp((E - E_F)/kT)} dE \quad (16)$$

where  $E_F$  is the Fermi level of the metal,  $g(E)$  the density of state (DOS) expressed in  $\text{mol m}^{-3} \text{J}^{-1}$ . The kinetics constants  $m_e^1$  and  $k_e^1$  are given by the Richardson average thermal velocity [36], i.e. respectively  $\sqrt{kT/2\pi m^*}$  and  $\sqrt{kT/2\pi m^{**}}$  where  $m^*$  and  $m^{**}$  are the effective mass of electron in the oxide and in the metal.

The DOS of iron and some others metals have been calculated in [37]. The variation of the DOS with energy is not regular but the integrated DOS variation with energy is roughly linear. So, it has been assumed that the DOS could be approximated as a constant called  $n_{DOS}$ . Similar situations occur for others metals like nickel, copper, etc. This corresponds to the Friedel model [38] generally accepted for transition metals. Using  $U = (E - E_F)/kT$  for integration  $c_e^{metal}$  is given by:

$$c_e^{metal} = kT n_{DOS} \int_{-(e\phi(X_1) + E_F)/kT}^{+\infty} \frac{dU}{1 + e^U} \quad (17)$$

Noticing that  $E_F = -eV_{free}$  at thermal equilibrium ( $J_e = 0$ ):

$$c_e^{metal} = kT n_{DOS} \ln[1 + \text{Exp}[-\gamma(V_{free} - \phi(X_1))]] \quad (18)$$

It has been assumed that (18) still stands when the metal is polarized, i.e.  $V \neq V_{free}$ . Introducing  $\Delta\phi_1 = V - \phi(X_1)$ , it must be noticed that when  $\Delta\phi_1$  is sufficiently negative,  $c_e^{metal} \approx -\gamma kT n_{DOS} \Delta\phi_1$ , i.e. the rate for injection of electrons from the metal to the oxide follows an Ohmic law. On the contrary for high positive values of  $\Delta\phi_1$ ,  $c_e^{metal} \approx kT n_{DOS} \text{Exp}[-\gamma \Delta\phi_1]$  which corresponds to a rectifying contact.

#### 3.2.4. Proton reduction

The net rate for this step is given by:

$$J_r = m_e^0 \sqrt{a_{H_2}} \exp(b_e^0 \gamma \phi(X_0)) - k_e^0 10^{-pH} c_e^0 \exp(-a_e^0 \gamma \phi(X_0)) \quad (19)$$

From a practical point of view, it's more convenient to introduce the redox potential of the solution rather the activity of hydrogen  $a_{H_2}$ . From the Nernst definition of the redox potential,  $\sqrt{a_{H_2}} = 10^{-pH} \exp(-\gamma E_{redox})$ . So:

$$J_r = m_e^0 10^{-pH} \exp(-\gamma E_{redox}) \exp(b_e^0 \gamma \phi(X_0)) - k_e^0 10^{-pH} c_e^0 \exp(-a_e^0 \gamma \phi(X_0)) \quad (20)$$

### 3.2.5. Ferrous release

As a consequence of the ferric release step, water is not the only oxidant in this scheme. Ferric cations in solution could be also reduced. The net rate is:

$$J_3 = m_r^0 a_{Fe^{2+}} \exp(a_r^0 \gamma \phi(X_0)) - k_r^0 a_{Fe^{3+}} c_e^0 \exp(-b_r^0 \gamma \phi(X_0)) \quad (21)$$

Both water reduction and ferrous release steps involve electrons in the oxide at the outer interface. So, the net flux  $J_e(X_0)$  is:

$$J_e(X_0) = J_3 + J_r \quad (22)$$

### 3.2.6. Oxide host lattice growth

The PDM [1] and the MCM [12] assume that the oxide growth step runs at the inner interface and produce oxygen vacancies that will be consumed at the outer interface. In MCM [12], the growth step is:



This equation describes the motion of the inner interface of the oxide layer, i.e. the motion of oxide anions. In this case, the Kröger–Vink notation is ambiguous. From (23), the oxide film is built in without oxide anions but only with iron cations ( $Fe_{Fe}^X$ ). Let us consider a case where there is an accumulation of oxygen vacancies in the vicinity of the inner interface. In such a case, it is clear that the oxide film growth would be difficult if not impossible. The growth rate would decline or even vanish. Eq. (23) cannot describe such a situation because the growth rate is independent on the concentration of oxygen vacancies. Oxide anions have been introduced in the oxide host lattice growth step (see Fig. 3). Then, the corresponding interface motion equation is:

$$\frac{1}{\Omega_{Fe}} \frac{dX_1}{dt} = k_{ox}^1 \left( 1 - c_{V_o}^1 \frac{\Omega_{ox}}{4} \right)^{r_a} \exp[3a_{ox}^1 \gamma (V - \phi(X_1))] - m_{red}^1 \times \left( c_{V_o}^1 \frac{\Omega_{ox}}{4} \right)^{r_c} \exp[-3b_{red}^1 \gamma (V - \phi(X_1))] \quad (24)$$

where  $c_{V_o}^1$  is the concentration of oxygen vacancies in the anionic sub-lattice of the OHL at the inner interface and  $4/\Omega_{ox}$  is the standard concentration of oxide anions in pure magnetite. If there is an accumulation of oxygen vacancies at the inner interface, the activity of oxide anions would decrease. This is depicted by the term  $(1 - c_{V_o}^1 (\Omega_{ox}/4))$ . If the concentration of oxygen vacancies is very low, the activity of oxide anions will be equal to 1. Then, the first term of the right hand of (24) will be similar to those corresponding to the reaction (23). The second term corresponds to the backward reaction, i.e. redissolution of oxide in metal. The OHL growth step does not involve a single charge carrier but  $4V_o^{\bullet\bullet}$  and  $4O_o^X$ . It is therefore not an elementary step and two orders of reaction  $r_a$  and  $r_c$  have been introduced. In the  $k_{ox}^1$  direction, four oxygen vacancies are injected into the oxide layer whereas the inner interface drifts toward positive direction:

$$\frac{1}{\Omega_{Fe}} \frac{dX_1}{dt} = -4J_{V_o^{\bullet\bullet}}(X_1) \quad (25)$$

### 3.2.7. Oxygen exchange

The oxygen vacancies are exchanged at the outer interface. Their net flux is:

$$J_{V_o^{\bullet\bullet}}(X_0) = m_{ox}^0 10^{-2pH} \left( 1 - c_{V_o}^0 \frac{\Omega_{ox}}{4} \right) \exp[-2b_{ox}^0 \gamma \phi_0] - k_{ox}^0 \times \left( c_{V_o}^0 \frac{\Omega_{ox}}{4} \right) \exp[2a_{ox}^0 \gamma \phi_0] \quad (26)$$

There is no order of reaction because this step involves a single oxygen vacancy and a single anion oxide.

### 3.2.8. Oxide host lattice dissolution

Following the same way that in PDM and MCM, it has been assumed that the OHL could be dissolved by the proton in the solution. The net rate of the OHL dissolution step is given by:

$$v_d(t) = -\Omega_{ox} [m_d^0 a_{Fe^{3+}} \exp(5b_d^0 \gamma \phi(X_0)) - k_d^0 (pH) \exp(-5a_d^0 \gamma \phi(X_0))] \quad (27)$$

It must be remembered that the OHL  $[Fe_7O_4]^{5'}$  depicts a mesh of spinel iron oxide in which all octahedral sites are free. They would be filled by the iron oxidation step (cf. Fig. 3). The net charge of the OHL is  $-5$ .

$v_d$  is written as the difference between two Butler–Volmer laws. The first term in (27) corresponds to the precipitation of the OHL. Such a step is unlikely. This assumption is supported by the fact that it's well known that precipitation of corrosion products from cations and anions in solution leads to the growth of another over layer generally porous. This over layer could be made of ferrous hydroxide, well ordered magnetite, siderite in carbonated media, etc. [39]. Then, a more realistic expression would be:

$$v_d(t) = \Omega_{ox} k_d^0 (pH) \exp(-5a_d^0 \gamma \phi(X_0)) \quad (28)$$

It must be noticed that this step is the only irreversible step considered in the reaction path depicted in Fig. 3.

## 4. Link to the Mott–Schottky model

The reaction path presented above involves 13 kinetics constants and Butler–Volmer coefficients. To solve the Poisson and the Fick equations 11 parameters are involved. To test the possible numerical schemes to solve both together all equations, it is necessary to get sane values for the kinetics constants and parameters. Some could be taken from literature data (diffusion coefficients, dielectric constant, density of states, etc.). But the others must be evaluated. This evaluation is easier to perform in simplified situations. For this purpose, the system considered below has been restricted to the reaction path for electrons (cf. Fig. 3). Iron cations have been considered as static and their concentration as homogeneous except in Section 4.4. The oxide layer thickness has been taken as time independent. The numerical scheme to solve DPCM in steady-state conditions with fixed boundaries has been detailed elsewhere [40].

The input data for this modelling are the temperature  $T$ , the pH and the redox potential of the solution, the concentrations of ferrous  $a_{Fe^{2+}}^{sol}$  and ferric  $a_{Fe^{3+}}^{sol}$  cations in the solution, the thickness of the oxide layer  $L$  and the applied potential  $V$ . In most computations,  $T = 25^\circ C$  and  $pH = 7$ . The parameters used to solve the Poisson equation are listed in Table 1. The parameters used to solve the Fick equations are listed in Table 2. References are noted in brackets when the parameters have been found in literature.

Next section shows that in the simplest case, the concentration of electrons profiles exhibit an accumulation and a depletion layer

**Table 1**  
Parameters used to solve the Poisson equation.

$\chi$	$\rho_{\text{hl}}/\text{C m}^{-3}$	$\Gamma_0/\text{F m}^{-2}$	$\Delta\phi_0^{\text{pzc}}$ vs. SHE/V	$\Delta\phi_1^{\text{pzc}}/\text{V}$	$\Gamma_1/\text{F m}^{-2}$	$\Omega_{\text{ox}}/\text{m}^3 \text{ mol}^{-1}$ a
10 [46,47,49]	$-(5F/\Omega_{\text{ox}})$	1.4 [60]	-0.4	0	1.0	$4.474 \times 10^{-5}$

a Calculated from the molecular weight and the density of magnetite.

**Table 2**  
Parameters used to solve the Fick equations.

$D_e/\text{m}^2 \text{ s}^{-1}$ a	$m^*$	$k_r^0/\text{m}^4 \text{ mol}^{-1} \text{ s}^{-1}$	$k_e^0/\text{m s}^{-1}$	$m_e^0/\text{mol m}^{-2} \text{ s}^{-1}$	$a_e^0$	$b_e^0$
$10^{-6}$ [25]	1	$5.6\text{--}3.5 \times 10^{-5}$	$10^{-9}$	$4.364 \times 10^{10}$	0.5	0.5
$D_{\text{Fe}^{+III}}/\text{m}^2 \text{ s}^{-1}$	$m^{**}$	$n_{\text{DOS}}/\text{mol m}^{-3} \text{ J}^{-1}$	$k_{\text{Fe}}^0/\text{m s}^{-1}$	$m_{\text{Fe}}^0/\text{m s}^{-1}$	$a_{\text{Fe}}^0$	$b_{\text{Fe}}^0$
$10^{-20}$ [34]	1 [61]	$1.35 \times 10^{-24}$ [37]	1.0	n.d.	0.5	0.5
$m_r^0/\text{m s}^{-1}$	$a_r^0$	$b_r^0$	$k_{\text{Fe}}^1/\text{m s}^{-1}$	$m_{\text{Fe}}^1/\text{m s}^{-1}$	$a_{\text{Fe}}^1$	$b_{\text{Fe}}^1$
$1.1\text{--}1.8 \times 10^{-14}$	0.5	0.5	1.0	$10^{-3}$	0.5	0.5
$D_{V^{**}}/\text{m}^2 \text{ s}^{-1}$ b	$r_a$	$m_{\text{red}}^1/\text{mol m}^{-2} \text{ s}^{-1}$	$m_{\text{ox}}^0/\text{mol m}^{-2} \text{ s}^{-1}$	$k_{\text{ox}}^0/\text{mol m}^{-2} \text{ s}^{-1}$	$a_{\text{ox}}^1$	$a_{\text{ox}}^0$
$10^{-20}$	1	$10^{-6}$	$10^{-24}$	$10^{14}$	0.5	0.5
$k_d^0/\text{mol m}^{-2} \text{ s}^{-1}$	$r_c$	$k_{\text{ox}}^1/\text{mol m}^{-2} \text{ s}^{-1}$		$a_d^0$	$b_{\text{red}}^1$	$b_{\text{ox}}^0$
$10^{-24}$	1	$10^{-7}$		0.5	0.5	0.5

a  $D_e$  has been calculated with the Nernst–Einstein relation from value of the electronic mobility.

b  $D_{V^{**}}$  has been taken equal to  $D_{\text{Fe}^{+III}}$ . The same way has been taken up in [19].

as predicted by the Mott–Schottky model. Section 4.2 is devoted to the influence of  $\Delta\phi_0^{\text{pzc}}$  and  $\Gamma_0$  on the kinetics of the outer electron exchange steps. The way to chose the values of  $k_e^0$ ,  $m_e^0$ ,  $k_r^0$  and  $m_r^0$  is also detailed. Section 4.3 details the link between DPCM and the Mott–Schottky model. It is shown that the Mott–Schottky model could be extended to cases where electronic current flow through the oxide layer. Section 4.4 illustrates an example of deviation from the Mott–Schottky model and Section 4.5 is devoted to the influence of  $\Delta\phi_1^{\text{pzc}}$ .

#### 4.1. Irreversible proton reduction on magnetite

In this section, it has been assumed that the solution contains neither ferrous nor ferric cation ( $a_{\text{Fe}^{2+}} = a_{\text{Fe}^{3+}} = 0$ ). It has also been assumed that the proton reduction step was irreversible ( $m_e^0 = 0$ ). Then, the cathodic current density only depends on the value of  $k_e^0$ . Its value has been chosen in order to obtain a cathodic current density around  $-0.1 \text{ mA cm}^{-2}$  at  $V = -0.8 \text{ V/SHE}$ . Computations have been performed for several oxide layer thicknesses of magnetite ( $\delta = 0$ ). The number of points in the mesh used for the computations has been taken equal to 300 for  $L = 20$  and 200 nm and 3000 for  $L = 2$  and 20  $\mu\text{m}$ . The results are thickness independent.

An example of the potential and the electrons concentration profiles are presented respectively in Figs. 5 and 6. It can be seen that a space charge layer arises at the outer interface. The electrons concentration profile exhibited an accumulation layer in the cathodic range and a depletion layer in the anodic range (cf. Fig. 6). The growth of such a space charge layer is the main result of the Mott–Schottky model. The thickness of this space charge layer is independent of the layer thickness. The band bending diagram has been built in drawing  $-e(\phi(x) - V)$  vs. the deepness  $x$  for each applied potential  $V$ . This band bending diagram is presented in Fig. 7. Negative band bending is observed for applied potentials lower than  $V = \Delta\phi_0^{\text{pzc}}$  and positive band bending is observed for higher potentials. For this simplest situation, at  $V = \Delta\phi_0^{\text{pzc}}$  the charge carried by the solution is null as well as the field at the

outer interface (Gauss law). So, there would be no band bending at the outer interface at this potential. Then, it is also the flat band potential. As it can be seen below, it is not always the case.

#### 4.2. Evaluation of the rest potential

Let us consider the case where iron is covered with magnetite ( $\delta = 0$ ) and is immersed in a solution with a redox potential  $E_{\text{redox}}$  equal to the potential of zero charge  $\Delta\phi_0^{\text{pzc}}$ . In such a situation, the rest potential of the electrode would be equal to  $E_{\text{redox}}$ . At the rest potential, the net current density is null. So, the anodic current density would be the opposite of the cathodic current density. In a first step, it has been assumed that  $a_{\text{Fe}^{2+}} = a_{\text{Fe}^{3+}} = 0$ . Then, Eq. (21) vanishes. From Eq. (20), it was possible to determine the value for  $m_e^0$  which vanished the net current density at  $V_{\text{rest}} = \Delta\phi_0^{\text{pzc}}$ . The corresponding current density–potential (CDP) curve is drawn in Fig. 8 (dashed line) in Tafel representation. The corresponding value

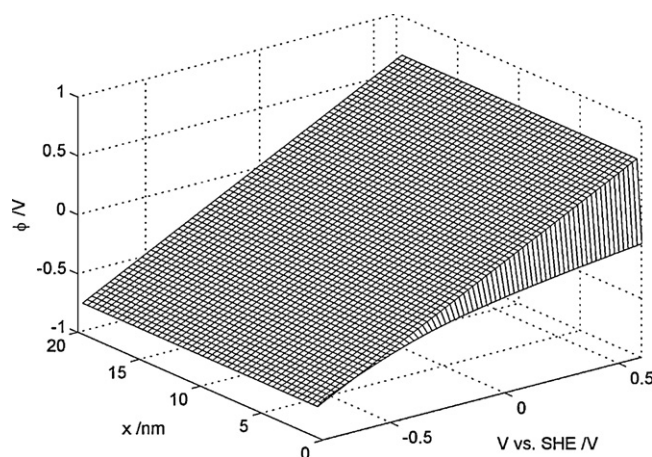


Fig. 5. Potential profile for magnetite.

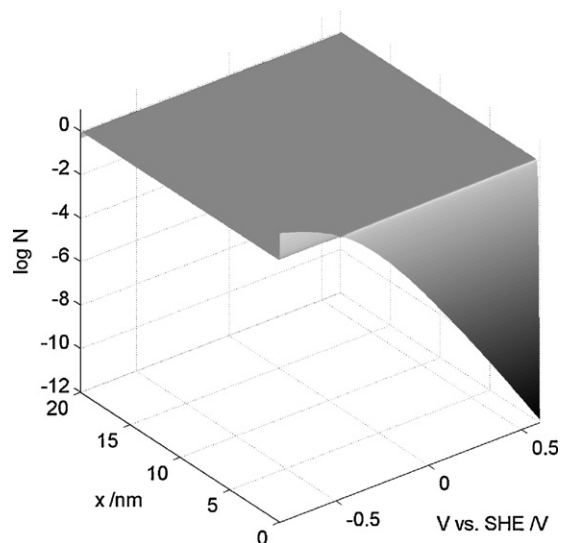


Fig. 6. Electrons concentration profile for magnetite.  $N(x) = c_e(x)\Omega_{ox}$  is the dimensionless concentration of electrons.

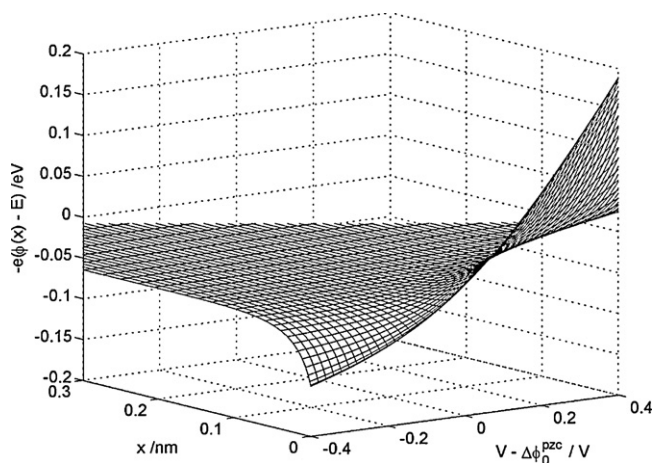


Fig. 7. Band bending at the outer interface around  $V = \Delta\phi_0^{pzc} = -0.4$  VSHE.

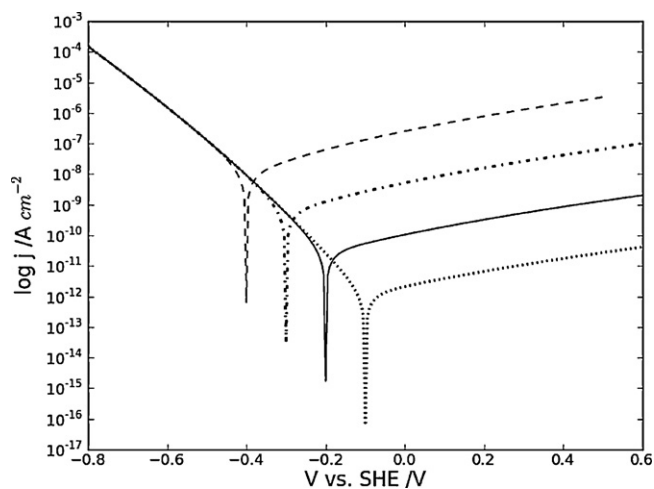


Fig. 8. Current density–potential curve for magnetite ( $\delta=0$ ) immersed in solution with:  $E_{redox} = -0.4$  V/SHE (dashed line),  $-0.3$  V/SHE (dashed-dotted line),  $-0.2$  V/SHE (solid line) and  $-0.1$  V/SHE (dotted line).

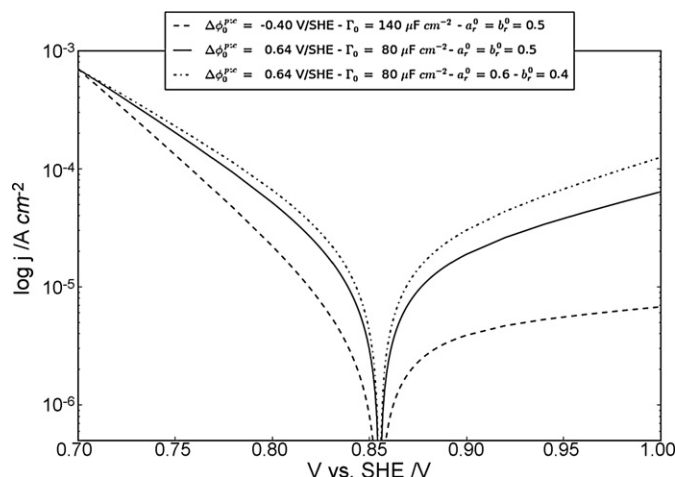


Fig. 9. Current density–potential curves in Tafel representation for a passive iron electrode immersed at  $40^\circ\text{C}$  in a solution containing  $0.3\text{ mol L}^{-1}$  of ferric cations and  $0.03\text{ mol L}^{-1}$  of ferrous cations in  $\text{H}_2\text{SO}_4$   $0.05\text{ mol L}^{-1}$  and  $\text{Na}_2\text{SO}_4$   $0.1\text{ mol L}^{-1}$ .

for  $m_e^0$  is listed in Table 2. Then, the CDP curves for others values of the redox potential could be calculated. These curves are depicted in Fig. 8. The rest potential of the magnetite/iron electrode is always equal to the redox potential of the solution.

The same way could be followed for the *ferrous release* step (cf. Fig. 3 and Eq. (21)). Makrides has published results concerning the kinetics of this step on a passive iron electrode in acid solution<sup>1</sup> [41]. From the experimental current density at  $V = +0.7$  V/SHE ( $j \approx -700\ \mu\text{A cm}^{-2}$ ), the value for  $k_f^0$  was determined. The value of  $m_f^0$  was adjusted so that the rest potential was equal to the redox potential ( $E_{redox} = +0.855$  V/SHE at  $40^\circ\text{C}$  [42]). The resulting CDP curve is drawn in Fig. 9 (dashed line). The overall order of magnitude is acceptable (see Fig. 3 in [41]), but discrepancies have arisen for the Tafel slopes. The cathodic and the anodic Tafel slopes estimated graphically from the dashed CDP in Fig. 9 were respectively  $-68$  and  $+492$  mV instead of  $-90$  mV ( $\alpha_c = 0.69$ ) and  $+270$  mV ( $\alpha_a = 0.23$ ) from [41]. The usual correction would be to change the values of the Butler–Volmer coefficients  $a_f^0$  and  $b_f^0$  in Eq. (21). But before to do that, another way could be tested.

Searson and coworkers [43] have shown that the seeming cathodic Tafel slope could be modified by the structure of the interface. These authors have used an equivalent electrical circuit to describe the sharing of voltage drops between the space charge layer and the Helmholtz layer. They have calculated that at  $25^\circ\text{C}$  the seeming cathodic Tafel slope increases from  $-118$  mV for the electron accumulation situation to  $-59$  mV for the deep electron depletion situation. Similar results have been obtained with DPCM and are presented in Fig. 10.<sup>2</sup> These curves could be normalized if they are plotted vs.  $\eta = V - \Delta\phi_0^{pzc}$ . The resulting curve depends only on the differential capacitance  $\Gamma_0$ . This dependence is depicted in Fig. 11. Equivalent results for the seeming anodic Tafel slope are presented respectively in Figs. 12 and 13.

The target of this section is to show how  $\Delta\phi_0^{pzc}$  and  $\Gamma_0$  may change the kinetic features of a simple redox reaction ( $\text{Fe}(\text{H}_2\text{O})^{2+/3+}$ ). This is qualitatively shown in Fig. 9. Using

<sup>1</sup> Iron immersed at  $40^\circ\text{C}$  in a solution containing  $0.3\text{ mol L}^{-1}$  of ferric cations and  $0.03\text{ mol L}^{-1}$  of ferrous cations in  $\text{H}_2\text{SO}_4$   $0.05\text{ mol L}^{-1}$  and  $\text{Na}_2\text{SO}_4$   $0.1\text{ mol L}^{-1}$ .

<sup>2</sup> These computations have been performed for a solution with the same pH and redox potential than those used in [41] but with a concentration in ferric cations lowered down to  $10^{-13}\text{ mol L}^{-1}$ . The ferric concentration used by Makrides ( $0.3\text{ mol L}^{-1}$ ) led to “very high” cathodic current densities ( $\approx 10^8\text{ A cm}^{-2}$ ) for  $V$  ranging from  $-0.6$  to  $-0.8$  V/SHE. This “very high” cathodic current density has no reality because limitation by diffusion would occur.

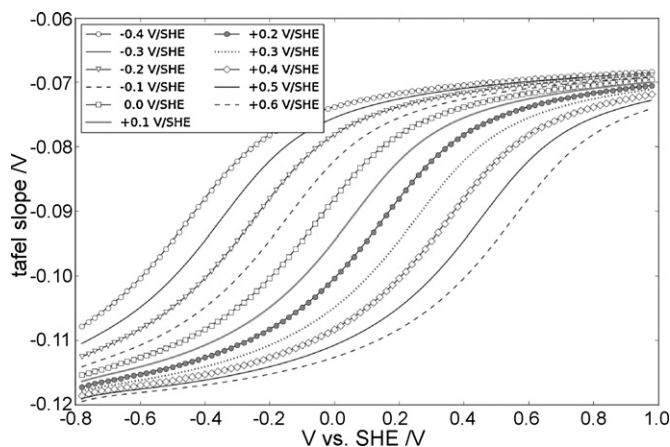


Fig. 10. Variations of the cathodic Tafel slope defined as  $dV/d \log j_c$  vs.  $V$  for several  $\Delta\phi_0^{pzc}$ .

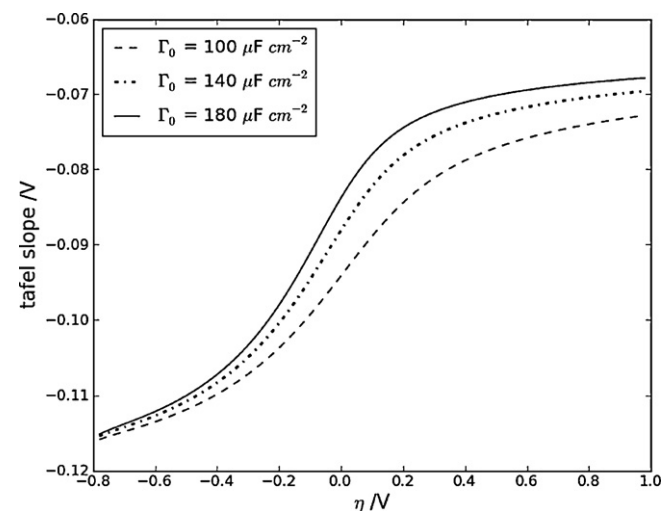


Fig. 11. Variations of the cathodic Tafel slope with the over voltage defined as  $\eta = V - \Delta\phi_0^{pzc}$  for different values of  $\Gamma_0$ .

Figs. 10–13 as guidelines, it was possible to estimate a couple of values for  $\Delta\phi_0^{pzc}$  and  $\Gamma_0$  which gave the good seeming cathodic Tafel slope, i.e.  $-90$  mV/decade. But the corresponding seeming anodic Tafel slope was only  $+210$  mV instead of  $+270$  mV. The two

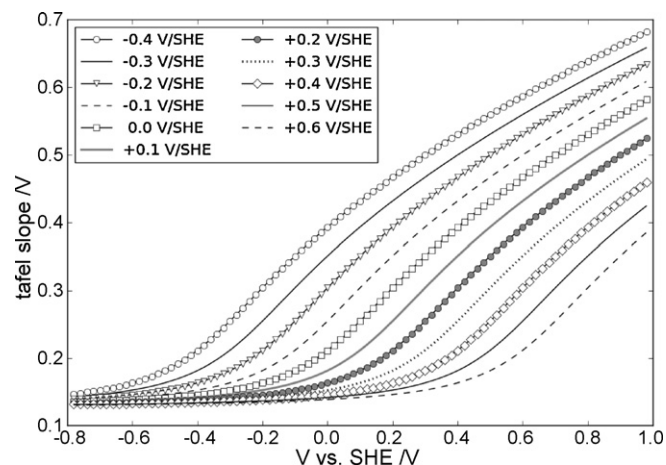


Fig. 12. Variations of the anodic Tafel slope defined as  $dV/d \log j_a$  vs.  $V$  for several  $\Delta\phi_0^{pzc}$ .

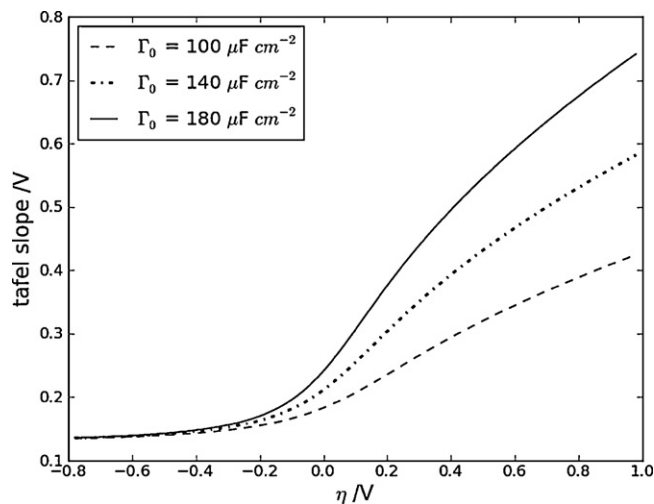


Fig. 13. Variations of the anodic Tafel slope with the over voltage defined as  $\eta = V - \Delta\phi_0^{pzc}$  for different values of  $\Gamma_0$ .

CDP curves have the same current density at  $V = +0.7$  V/SHE and the same rest potential.  $k_r^0$  and  $m_r^0$  were modified for this purpose. The Butler–Volmer theory for a one electron exchange reaction between two species in solution without adsorbed state ensures that  $a_r^0 + b_r^0 = 1$ . The above computations have been performed with  $a_r^0 = b_r^0 = 0.5$ . A computation has been performed with  $a_r^0 = 0.4$  and  $b_r^0 = 0.6$ . It is depicted in Fig. 9 (dot dashed curve). Comparison of the three curves in Fig. 9 illustrates that  $\Delta\phi_0^{pzc}$  and  $\Gamma_0$  could change the shape of the CDP in the same way than  $a_r^0$  and  $b_r^0$ . This shows that such kinetic experiment must be coupled with another experiment which characterizes the structure of the interface. One possible experiment could be the Mott–Schottky experiment which allows evaluating the flat band potential which is linked to  $\Delta\phi_0^{pzc}$ .

#### 4.3. Influence of the stoichiometry of the oxide

In this section, the stoichiometry  $\delta$  of the oxide has been changed in the range  $0 \leq \delta \leq (1/3)$ . The lower and the upper limits correspond respectively to the magnetite and to the maghemite. The redox potential of the solution has been fixed to  $-0.2$  V/SHE<sup>3</sup> [44]. It has been assumed that  $a_{Fe^{2+}} = a_{Fe^{3+}} = 0$ . The layer thickness was  $L = 20$  nm. The value of  $m_e^0$  was determined in previous section. The CDP curves are depicted in Fig. 14 in Tafel representation. The rest potential increased slightly with  $\delta$  ( $\approx 20$  mV). The shape of the CDP curve changed slightly with  $\delta$  in the cathodic range. The most noticeable change concerned the anodic range. The slope and the level of the CDP curve decreased as  $\delta$  increased. For maghemite ( $\delta = 1/3$ ), the anodic part of the curve was flat. This shape corresponds to a n-type Schottky diode.

The variations of  $\Delta\phi_0$  vs.  $V$  are presented in Fig. 15. From (6) and for  $\Gamma_0$  constant, the charge carried by the solution  $\sigma_0$  is given by:

$$\sigma_0 = -\Gamma_0(\Delta\phi_0 - \Delta\phi_0^{pzc}) \quad (29)$$

The differential capacitance  $C$  of the electrode is defined as the derivative of the charge carried by the solid phase vs. the applied potential  $V$ . This net charge is the sum of charges contained in the oxide layer and the charge carried by the metal ( $\sigma_1$ ). It has been shown that DPCM always ensures the net electroneutrality of the whole solution–oxide layer–metal system (see Eq. (8)). The charge

<sup>3</sup> This value corresponds roughly to the redox potential calculated by Gaucher et al. [44] for the geological clay layer in which nuclear waste would be disposed (the callovian-Oxfordian formation under Bure in France).

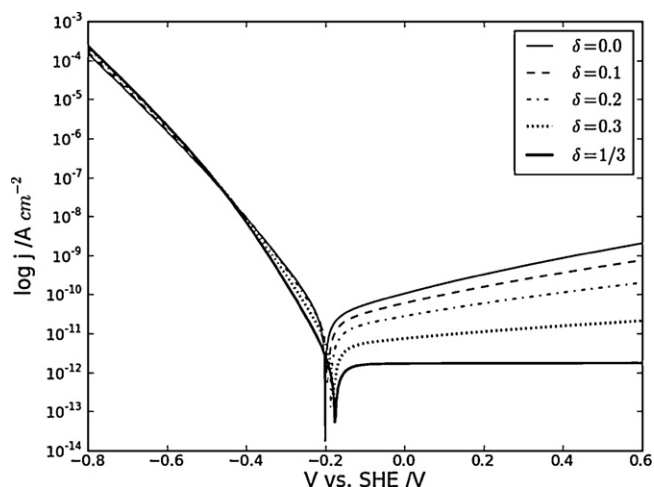


**Fig. 14.** Current density–potential curves obtained in a solution with  $E_{redox} = -0.2$  V/SHE for different values of the stoichiometry  $\delta$  ( $\text{Fe}_{3-\delta}\text{O}_4$ ).

carried by the solid phase is thus equal to the opposite of the charge carried by the solution ( $-\sigma_0$ ). The simplest way to calculate the differential capacitance  $C$  of the solid phase is therefore to use the following relation:

$$C(V) = -\frac{\partial \sigma_0}{\partial V} = \Gamma_0 \frac{\partial \Delta \phi_0}{\partial V} = \alpha(V) \Gamma_0 \quad (30)$$

$\alpha(V)$  is the derivative of curves drawn in Fig. 15 and are plotted in Fig. 16. From (30), the Mott–Schottky plots were calculated and are shown in Fig. 17. A straight line was observed for  $V > -0.4$  V/SHE ( $\Delta \phi_0^{pzc}$ ). The slope of the straight line increased with  $\delta$ . This means that the donor density  $N_d$  decreased as  $\delta$  increased. For  $\delta = 1/3$ , the slope  $\alpha(V)$  decreased to zero for  $V > -0.2$  V/SHE (cf. Fig. 16). The variation of  $C(V)$  is shown in Fig. 18. In the anodic potential range, the differential capacitance  $C$  was potential independent and equal to the geometrical capacitance  $C = \chi \chi_0 / L$ .

The Mott–Schottky model assumes that the electrons inside the semiconductor are in thermal equilibrium, i.e. no current flows through it. It must be outlined that DPCM allows extending Mott–Schottky in cases where anodic current pass through the whole system (cf. Fig. 14). Similar straight lines were obtained for  $V > \Delta \phi_0^{pzc}$  in the calculations of Section 4.2 (cf. Fig. 9).

The slope of the straight line on the Mott–Schottky plot allows calculating the donor density  $N_d$ . The results are plotted in the

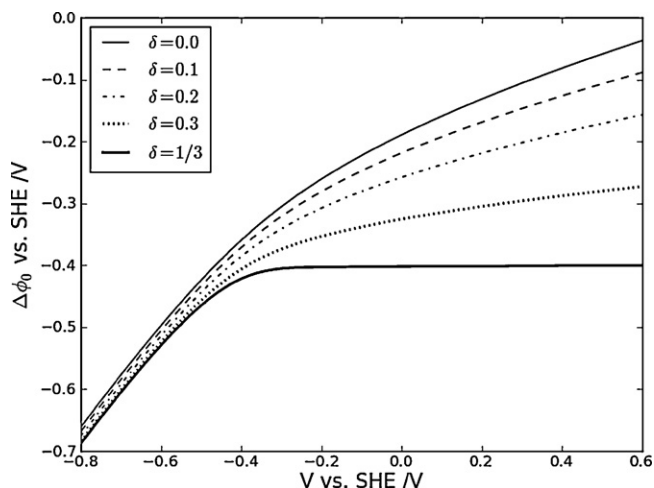


**Fig. 15.** Evolution of the outer voltage drop  $\Delta \phi_0$  with the applied potential  $E$  for different value of the stoichiometry  $\delta$  of the oxide  $\text{Fe}_{3-\delta}\text{O}_4$ .

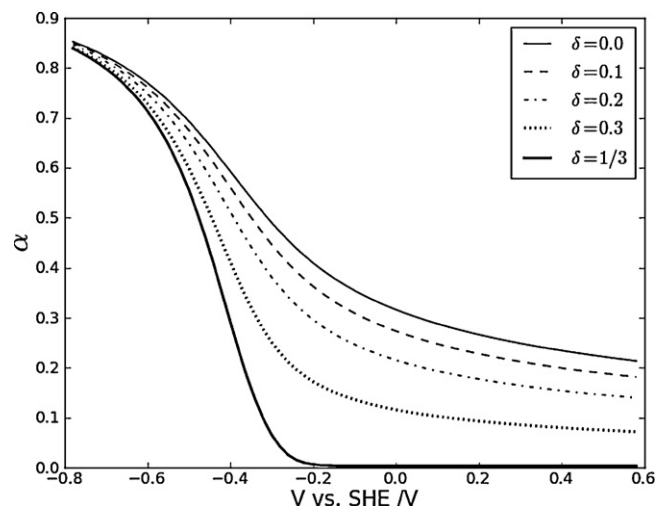


**Fig. 16.** Evolution of the derivative  $\alpha = \partial \Delta \phi_0 / \partial V$  with the applied potential  $V$ .

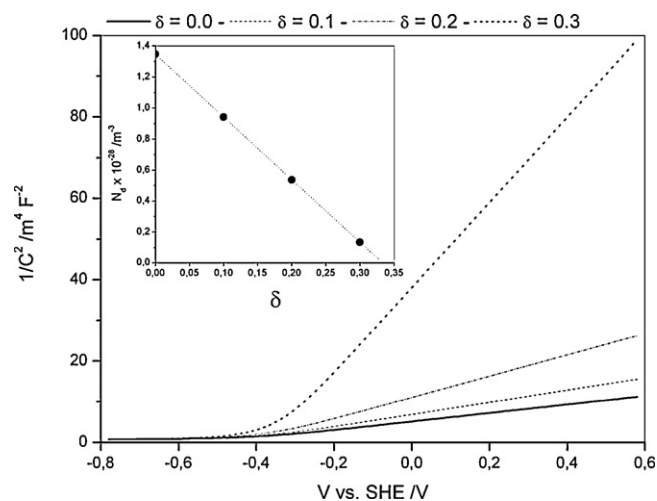


**Fig. 17.** Mott–Schottky plots obtained for different values of the stoichiometry  $\delta$  in  $\text{Fe}_{3-\delta}\text{O}_4$ . In the inset: variations of the donor density  $N_d$  calculated from the Mott–Schottky plot with the stoichiometry  $\delta$  ( $\text{Fe}_{3-\delta}\text{O}_4$ ).

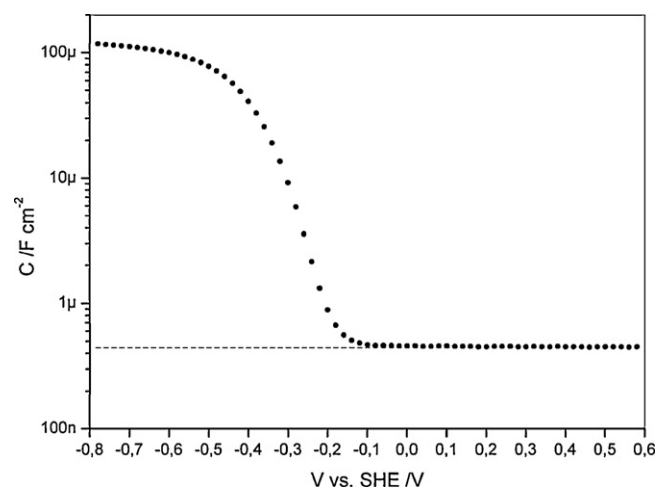


**Fig. 18.** Variations of the differential capacitance for the maghemite ( $\delta = 1/3$ ). The dashed line corresponds to the geometrical capacitance  $C = \chi \chi_0 / L$ .

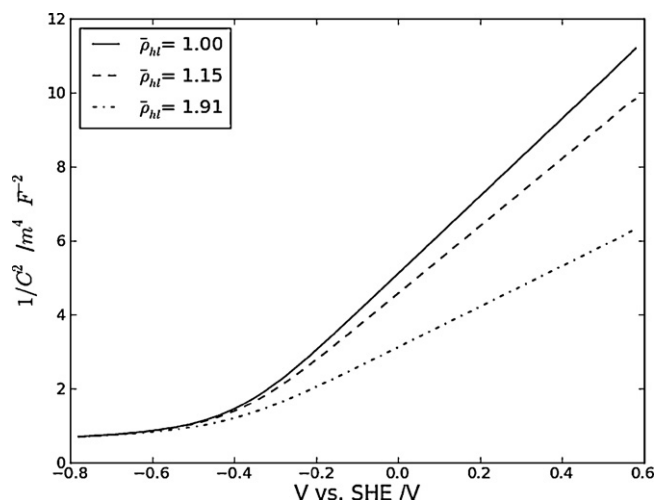


Fig. 19. Calculated Mott–Schottky plots for different values of the dimensionless host lattice charge  $\bar{\rho}_{hl}$ .

inset of Fig. 17. As expected, the donor density  $N_d$  decreased when  $\delta$  increased. The relationship was linear and  $N_d$  vanished for maghemite ( $\delta = 1/3$ ). As pointed out by Schmuki et al. [45], magnetite could be considered as maghemite  $\gamma\text{-Fe}_2\text{O}_3$  doped with  $\text{Fe}^{+III}$  completely ionized ( $\text{Fe}^{+III}$ ).

For magnetite ( $\delta = 0$ ),  $N_d = 1.345 \times 10^{28} \text{ m}^{-3}$ . This value falls between those obtained by Buchler et al. [46] and Castro et al. [47]. Buchler et al. have studied magnetite layer (500 nm thick) deposited by RF-magnetron sputtering on gold/copper substrate.<sup>4</sup> These authors have obtained  $N_d = 4.2 \times 10^{27} \text{ m}^{-3}$ . This value was about three times lower than those calculated here. It must be outlined that the magnetite layer was deposited in using  $\text{Fe}_2\text{O}_3$  target under conditions where hematite would be reduced to magnetite. From the results gathered in Fig. 18, a possible explanation would be that the reduction in magnetite would not be complete ( $\delta \approx 0.22$ ). These computations have been performed for  $L = 20 \text{ nm}$  and  $L = 500 \text{ nm}$  to check that the value of  $N_d$  was well independent of the thickness.

On the other side, Castro et al. [47] have studied a geological magnetite (from the Argentine collection) mounted on disc electrode. For  $\text{pH} = 8.4$ , Castro et al. have measured  $N_d = 3.7 \times 10^{28} \text{ m}^{-3}$ . This value was about three times higher than those calculated here. A possible explanation could come from the geological origin of this magnetite. An EDAX analysis has revealed that this magnetite was not pure. It contained 20% of Al and 15% of Si [48]. Unfortunately, these authors have omitted to precise if the percents were expressed in atom or in mass. Let us consider a doped magnetite  $[\text{Al}_{0.2}^{+III}\text{Si}_{0.15}^{+IV}\text{Fe}_{2.65}^{+III}\text{O}_4]^{1.15\bullet}(n\bar{e})$ ; the dimensionless charge of the host lattice is 1.15. If a percentage in mass was considered, the formula would become  $[\text{Al}_{1.26}^{+III}\text{Si}_{0.91}^{+IV}\text{Fe}_{0.82}^{+III}\text{O}_4]^{1.91\bullet}(n\bar{e})$ . The dimensionless charge of the host lattice would then be 1.91. Computations with these host lattice charges  $\bar{\rho}_{hl} = \rho_{hl}(\Omega_{ox}/F)$  have been performed. The results are presented in Fig. 19. The case of pure magnetite  $\bar{\rho}_{hl} = 1$  is also presented for comparison. The slope decreased when  $\bar{\rho}_{hl}$  increased. But even for the highest value ( $\bar{\rho}_{hl} = 1.91$ ),  $N_d = 2.572 \times 10^{28} \text{ m}^{-3}$ . This value was still lower than those measured by Castro et al. Another possible explanation would be that the dielectric constant  $\chi$  of the oxide used to calculate  $N_d$  would be inaccurate. In fact, the value is generally chosen from the literature ( $\chi = 10$ ). To test this way, some computations have been

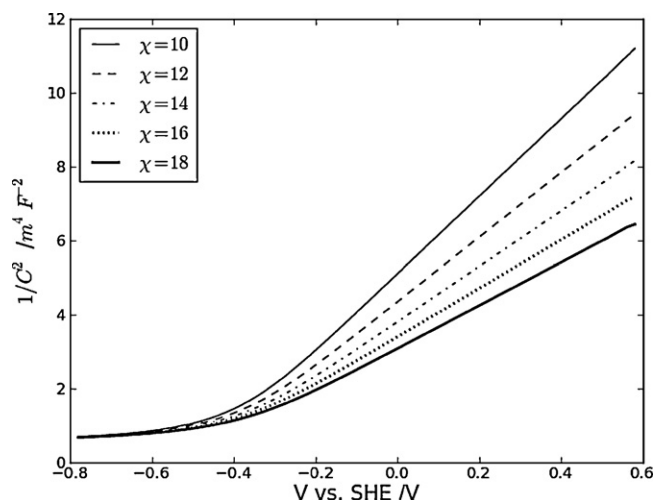


Fig. 20. Calculated Mott–Schottky plots obtained for different values of the dielectric constant  $\chi$  for the oxide.

performed in changing  $\chi$  in Eqs. (3) and (4) and keeping  $\bar{\rho}_{hl} = 1$ . The results are plotted in Fig. 20. The slope of the straight line of the Mott–Schottky plot decreased when  $\chi$  increases. From the slope of the straight line, the value of  $N_d$  has been calculated taking a value for the dielectric constant always equal to 10. For the highest value ( $\chi = 18$ ),  $N_d = 2.423 \times 10^{28} \text{ m}^{-3}$ . It is likely that the high value measured by Castro et al. would result from both effects. The substitution of  $\text{Fe}^{+III}$  by  $\text{Si}^{+IV}$  leads to an increase of the host lattice charge  $\bar{\rho}_{hl}$  and the dielectric constant  $\chi$  would be higher than 10 because this magnetite was not pure (Al = 20% and Si = 15%).

#### 4.4. Influence of non-homogeneous cations profiles

The aim of this section was to simulate a standard Mott–Schottky experiment. In such experiment, the passive film grows under potentiostatic condition ( $V = V_{\text{form}}$ ) until a quasi-stationary state is reached. Then, the applied potential  $V$  is scanned to get the capacitance  $C$  vs.  $V$  curve. The scan rate is chosen sufficiently high to avoid changes in film features (thickness, etc.) but not too high to allow the electrons profile to reach the corresponding  $V$  steady-state. In practice, such simulations were similar to those presented in the previous section except for the cations concentration profiles which were not homogeneous. These profiles have been built in with DPCM. The formula of the oxide was  $[\text{Fe}_7\text{O}_4]^{5\bullet}(n\bar{e}, (2 - \delta)\text{Fe}_0^{+III})$ . From [34],  $D_{\text{Fe}^{+III}} = 10^{-20} \text{ m}^2 \text{ s}^{-2}$  at room temperature. This value is in agreement with those used by Bojinov et al. [12]. This diffusion coefficient is 10 orders of magnitude lower than those of electrons. This difference justifies the way to perform the calculations, i.e. to compute for each  $V$  the steady-state potential and the concentration of electrons profiles keeping the cations concentration profile fixed to the one obtained previously for the steady-state at  $V_{\text{form}}$ .

In this section,  $a_{\text{Fe}^{3+}}$  has been assumed null for simplicity. In a first step, computations have been performed with several values for  $k_{\text{Fe}}^0$  in changing the ratio  $m_{\text{Fe}}^1/k_{\text{Fe}}^1$ . The results appeared to be insensitive to the value of this ratio as far as it was lower than  $10^{-2}$ . For simplicity,  $k_{\text{Fe}}^1 = 1 \text{ m s}^{-1}$  and  $m_{\text{Fe}}^1 = 10^{-3} \text{ m s}^{-1}$  have been chosen to continue the computations. In this condition, the level of the anodic part of the CDP curve was monitored only by the value of  $k_{\text{Fe}}^0$ . Its value has been chosen in order to obtain a free corrosion potential around  $-0.5 \text{ V/SHE}$  ( $V_{\text{corr.}} = -0.511 \text{ V/SHE}$  ( $k_{\text{Fe}}^0 = 1 \text{ m s}^{-1}$ )).

In a second step, the computations have been performed for 3 layer thicknesses ( $L = 2.5, 5$  and  $10 \text{ nm}$ ). The corresponding CDP curves are depicted in Fig. 21. Only the anodic part of the CDP

<sup>4</sup> The Mott–Schottky measurements have been performed at room temperature in borate buffer solution ( $\text{pH} = 8.4$ ).

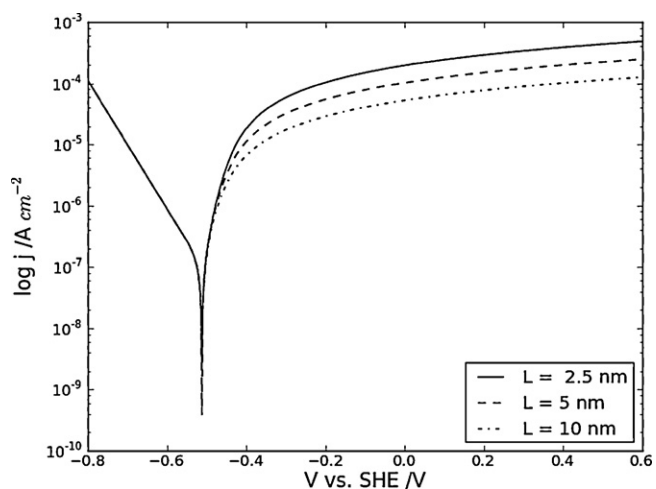


Fig. 21. Current density–potential curves for several thicknesses in Tafel representation.

was changed. Its intensity decreased as the thickness increased. An example of steady-state non-homogeneous iron cations concentration profiles are presented in Fig. 22 for  $L = 5$  nm. These profiles were homogeneous except in the vicinity of the inner and the outer interfaces. For each applied  $V_{form}$ , integration along the  $x$ -axis gave the mean stoichiometry of the oxide layer:

$$\langle P \rangle = \frac{1}{L} \int_0^L P(x) dx = 2 - \delta \quad (31)$$

where  $P$  is the dimensionless iron cations concentration  $P = c_{Fe} \Omega_{ox}$ . The variations of  $\delta$  with  $V_{form}$  are shown in Fig. 23. It was observed that  $\delta$  decreased with  $V_{form}$  from maghemite ( $\delta = 1/3$ ) for anodic applied potential to oxidized magnetite in the cathodic range ( $\delta \approx 0.25$ ).

Six values of  $V_{form}$  have been chosen. They are listed in the inset of Figs. 24 and 25. The Mott–Schottky plots have been built in as in Section 4.3 (Eq. (30)). The results are presented in Figs. 24 and 25. For the three thicknesses, the shapes of the Mott–Schottky plots were quite similar. The plot for  $L = 10$  nm is not shown here. For  $V_{form} = -0.4$  V/SHE, the expected shape of the Mott–Schottky plot has been obtained. For higher values of  $V_{form}$ , a steep increase is observed for  $V > -0.3$  V/SHE followed by a flattening variation. Such a deviation has been already observed in literature [49–53].

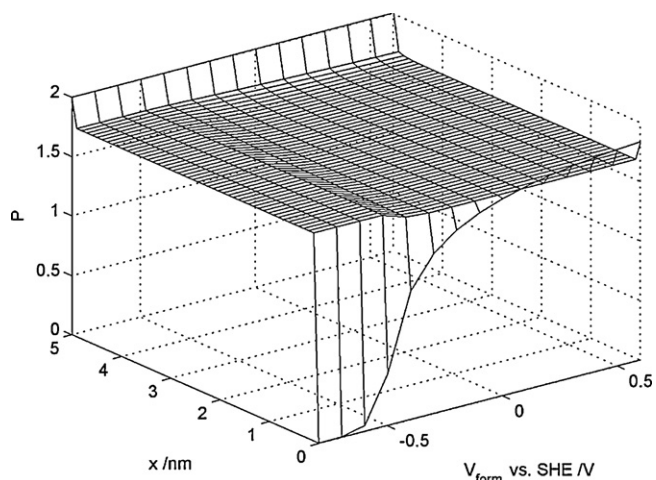


Fig. 22. Dimensionless iron cations concentration profiles for several applied  $V_{form}$ .  $P = c_{Fe} \Omega_{ox}$ .

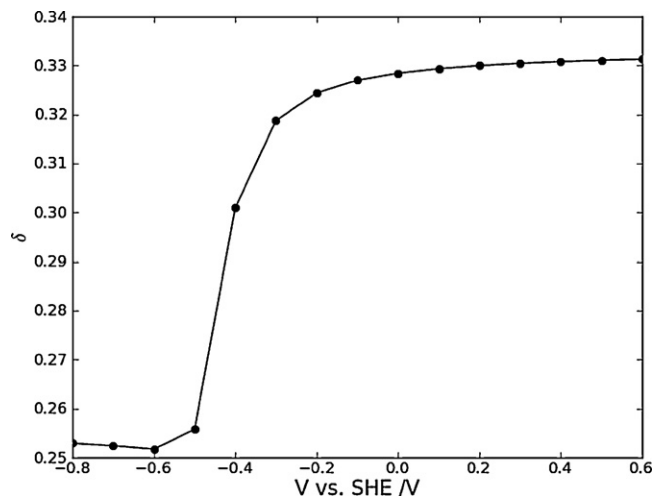


Fig. 23. Evolution of  $\delta$  in  $Fe_{3-\delta}O_4$  with the applied potential  $V_{form}$  ( $L = 5$  nm).

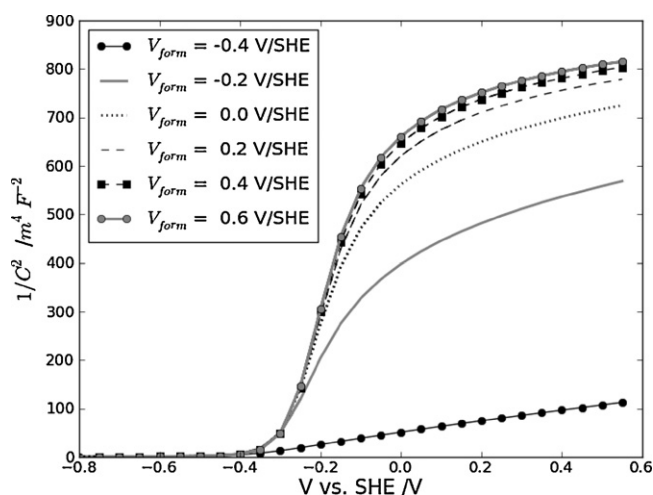


Fig. 24. Mott–Schottky plot obtained for  $L = 2.5$  nm and for several applied potential  $V_{form}$ .

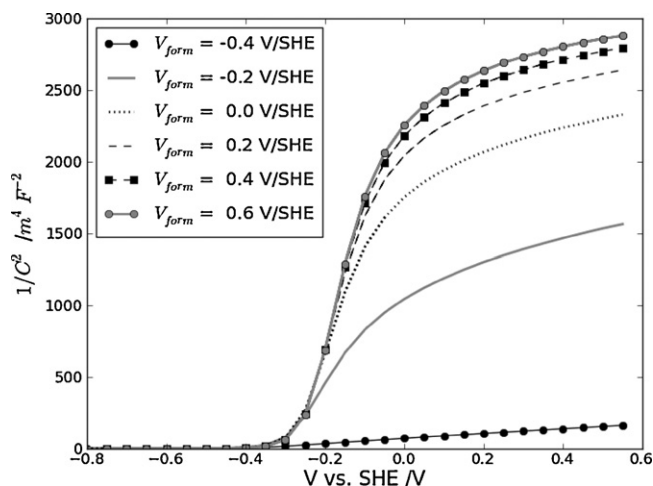


Fig. 25. Mott–Schottky plot obtained for  $L = 5$  nm and for several applied potential  $V_{form}$ .

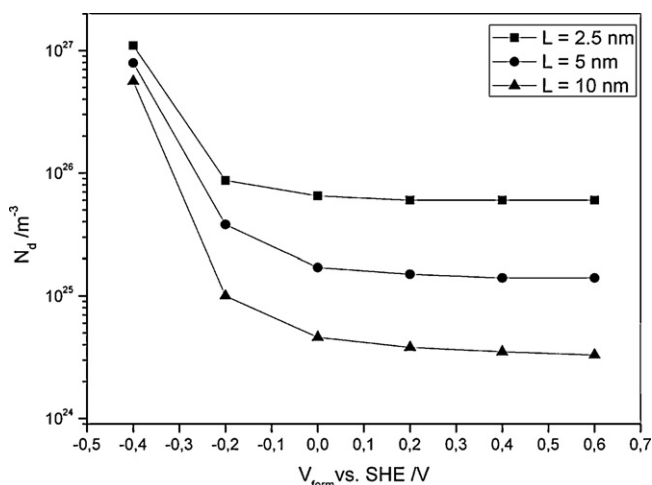


Fig. 26. Evaluation of the donor density  $N_d$  for different  $V_{\text{form}}$  and different thicknesses.

Stimming and Schultze [50] have performed capacity measurements on passivated iron by the potentiostatic pulse method in dependence on the oxide layer thickness and on the potential borate buffer. He has found that  $C^{-2}$  was roughly proportional to the square oxide layer thickness in the range 1.7–2.7 nm. Similar trend has been obtained with DPCM. Comparing Figs. 24 and 25, it must be noticed that the scale of the ordinate increases as  $L$  increases.

Even if there was a considerable deviation from linearity, it is always possible to evaluate the seeming donor density  $N_d$  from the slope of the linear part at the bottom of the steep increase. These evaluations are plotted in Fig. 26. The estimated values of  $N_d$  increased as the thickness of the oxide layer decreased and as the potential  $V_{\text{form}}$  decreased. At high  $V_{\text{form}}$ , the value of  $N_d$  was less potential dependent. It tended toward a plateau. The latter trend was in qualitative agreement with the experimental results published by Sikora and MacDonald [49] concerning the passive film formed on iron in borate buffer.

#### 4.5. Influence of the inner potential of zero charge

The potential  $\Delta\phi_1^{\text{pzc}}$  corresponds to a voltage drop at the inner interface when the charge carried by the metal is null. The border field given by the Gauss law is also null, i.e. there is no band bending at this interface. This voltage drop is linked to the difference between the Fermi levels of the metal and the oxide. The Fermi level in a semiconductor is defined as [54]:

$$E_F^{\text{oxide}} = E_{bc} + kT \ln \frac{c_e}{N_d} \quad (32)$$

where  $E_{bc}$  is the energy level of the conduction band. When there is no band bending at the inner interface, the local electroneutrality stands near this interface. The concentration of electrons is equal to the concentration of donors  $N_d$ . Then, the Fermi level in the oxide  $E_F^{\text{oxide}}$  at the inner interface is equal to the energy level of the conduction band  $E_{bc}$ . In other words,  $-e\Delta\phi_1^{\text{pzc}}$  corresponds to the work function introduced by Fromhold and Cook [55] in their modelling (FCM) of gaseous oxidation of metal covered by a thin oxide layer 2–5 nm thick. The aim of this section was to study the influence of  $\Delta\phi_1^{\text{pzc}}$  on the kinetics and the electrostatic features of the simple system under consideration here. The parameters and kinetics constants used in this section were the same than those used in Section 4.3. The stoichiometry of the oxide has been fixed homogeneous to those of the magnetite ( $\delta=0$ ) and to those of a slightly reduced maghemite  $\text{Fe}_{2.667}\text{O}_4$ . The influence of  $\Delta\phi_1^{\text{pzc}}$  on the CDP curves in Tafel representation is depicted in Figs. 27 and 28. A pos-

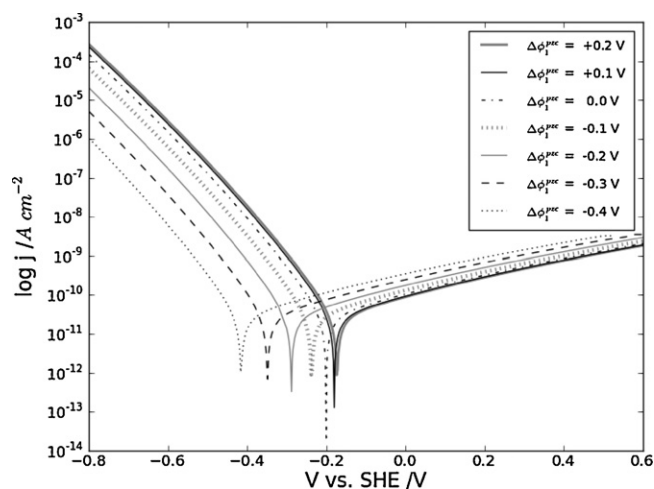


Fig. 27. Variation of the current density–potential curves with  $\Delta\phi_1^{\text{pzc}}$  in Tafel representation for magnetite.

itive increase of  $\Delta\phi_1^{\text{pzc}}$  did not change much a lot the CDP curve. On the contrary, a negative change led to a decrease of the cathodic part of the CDP curve and to a slight increase of the anodic part for magnetite. It must be outlined that the level of the cathodic branch in the Tafel representation depends on one side of the value for  $k_e^0$  and on the other side on the value of  $\Delta\phi_1^{\text{pzc}}$ . It would be always possible to find a couple of values which will give the same cathodic branch.

The Mott–Schottky plots are represented in Figs. 29 and 30. It can be seen that the slope of the straight line was not affected by  $\Delta\phi_1^{\text{pzc}}$ . On the contrary, the flat band potential  $V_{\text{fb}}$  is shifted. This shift is plotted in Fig. 31 for magnetite. For comparison, the potential  $V_0^{\text{pzc}}$  for which  $\Delta\phi_0 = \Delta\phi_0^{\text{pzc}}$  is also plotted. This latter potential is the true flat band potential because the field at the outer interface is null; therefore no band bending occurs. For slightly reduced maghemite, a similar shift was observed (cf. Fig. 32), but  $V_0^{\text{pzc}}$  were equal to  $V_{\text{fb}}$ . The shift between  $V_{\text{fb}}$  and  $V_0^{\text{pzc}}$  has been emphasized [43,56] to occur when the space charge layer capacitance is too high and not negligible in front of  $\Gamma_0$ . This was actually the case for magnetite but not for the slightly reduced maghemite for which the value of the space charge layer capacitance was about 30 times lower than the one for magnetite (cf. Figs. 29 and 30).

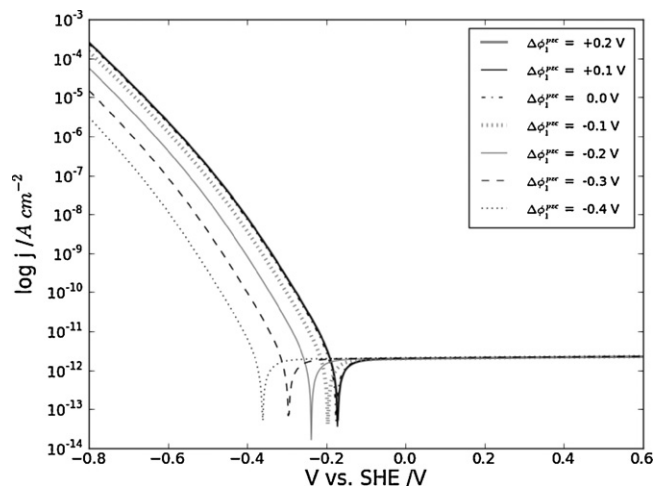


Fig. 28. Variation of the current density–potential curves with  $\Delta\phi_1^{\text{pzc}}$  in Tafel representation for slightly reduced maghemite  $\text{Fe}_{2.667}\text{O}_4$ .

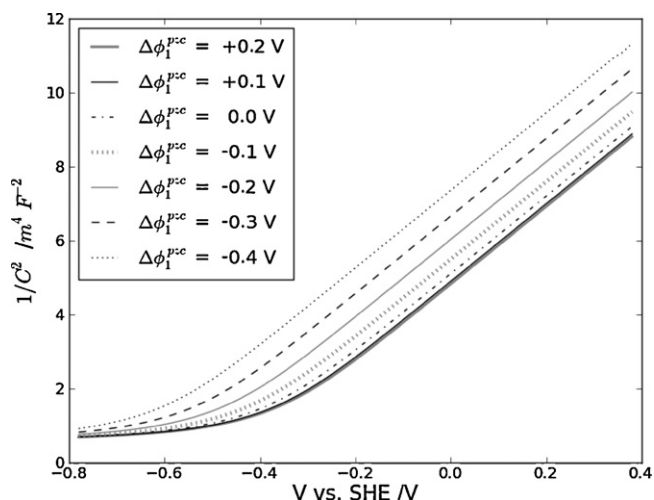


Fig. 29. Variations of the Mott-Schottky plots with  $\Delta\phi_1^{pzc}$  for magnetite.

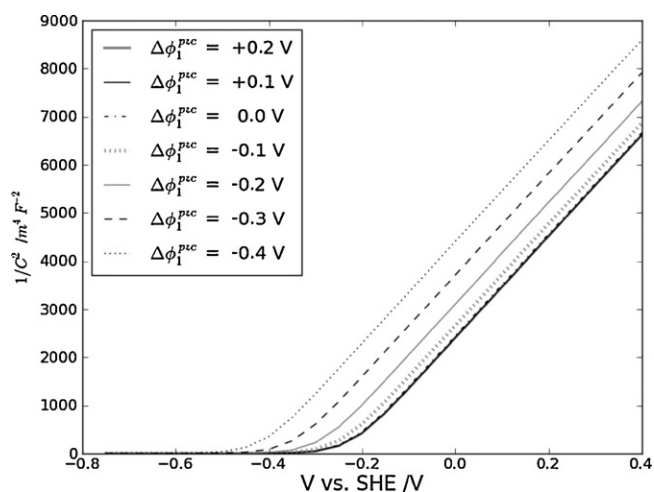


Fig. 30. Variations of the Mott-Schottky plots with  $\Delta\phi_1^{pzc}$  for slightly reduced maghemite  $\text{Fe}_{2.667}\text{O}_4$ .

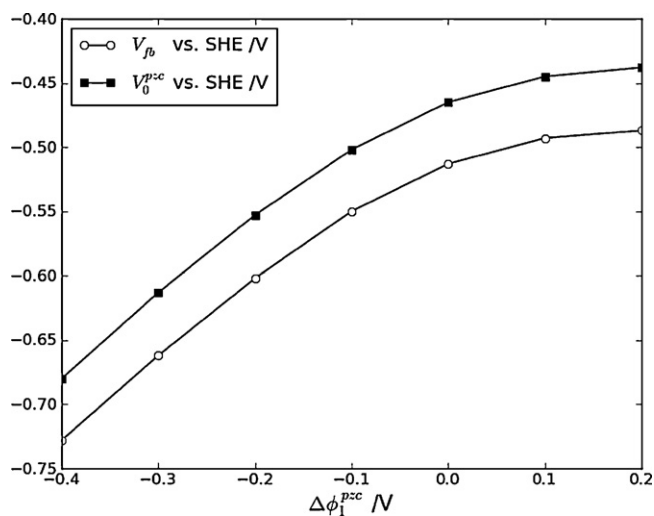


Fig. 31. Variations of the flat band potential  $V_{fb}$  deduced from the Mott-Schottky plots of Fig. 29 for magnetite and of the potential of zero charge  $V_0^{pzc}$  (see text for definition).

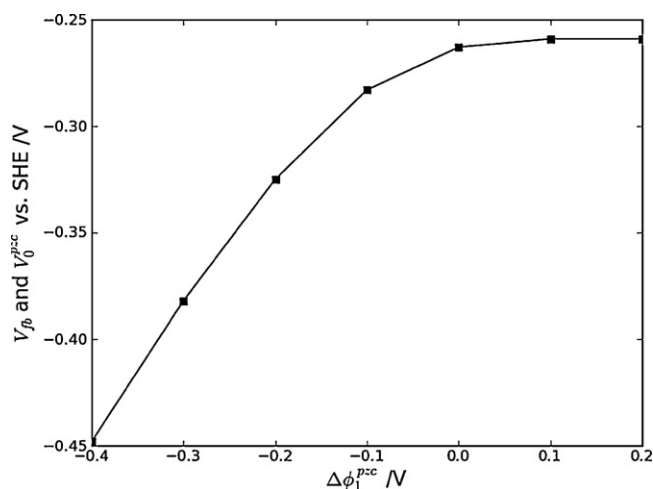


Fig. 32. Variations of the flat band potential  $V_{fb}$  deduced from the Mott-Schottky plots of Fig. 30 for slightly reduced maghemite.

The shift of  $V_0^{pzc}$  could be due to the charge carried by the iron. This charge depends on the difference between  $\Delta\phi_1$  and  $\Delta\phi_1^{pzc}$ . The value of  $\Delta\phi_1$  was monitored by the kinetics at the inner interface. As a consequence,  $V_0^{pzc}$  would be also monitored by the kinetics. As the CDP curve did not change much a lot for positive value of  $\Delta\phi_1^{pzc}$ , the value of  $V_0^{pzc}$  did not change much as well. On the contrary, as the CDP curve changed with negative values of  $\Delta\phi_1^{pzc}$ , the change of  $V_0^{pzc}$  was more significant. Unfortunately, there was no analytical expression able to depict this change. This result shows that the interpretation of values measured for  $V_{fb}$  could be complicated because it could be dependent on a large number of parameters which are not necessarily known.

## 5. Oxide layer growth

The purpose of this section is to simulate the growth of the oxide layer. The paper of Szklarska-Smialowska and Kazlowski [57] was used as a guideline (especially Fig. 5 herein). These authors have studied by ellipsometry, the growth of the passive layer on iron in borate buffer at room temperature as a function of applied potential during 1 h.

In a first step, the value of the kinetic constant  $k_d^0$  for the *oxide host lattice dissolution* reaction was set to zero. The initial thickness of the film has been always fixed to 1 nm. Calculations were made in order to obtain growth curves of the same order of magnitude in thickness and time than those presented in Fig. 5 in [57]. This helped to choose some values of kinetic constants for the *oxide host lattice growth* and the *oxygen exchange* reactions. These values are given in Table 2. In a second step, calculations were made by increasing the value of  $k_d^0$ . An example result is shown in Fig. 33. For low values of  $k_d^0$ , the growth of the oxide layer is monotonous over the duration of the simulation (1 h). For higher values of  $k_d^0$ , a steady-state thickness was reached. The higher the value of  $k_d^0$  was, the lower the steady-state thickness was and the quicker it was reached. Measures performed by Szklarska-Smialowska and Kazlowski [57] showed that steady-state thickness was never reached after 1 h of polarization. To be in agreement with this statement, the value of  $k_d^0$  was set to  $10^{-24} \text{ mol m}^{-2} \text{ s}^{-1}$ . Then, the duration of calculations has been increased to 10 h. The evolution of the oxide layer thickness with time for different values of the applied potential  $V$  is shown in Fig. 34. For all applied potentials used for these calculations, a steady-state thickness was reached between 1 and 10 h. This thickness was potential dependent. The variation of this steady-state

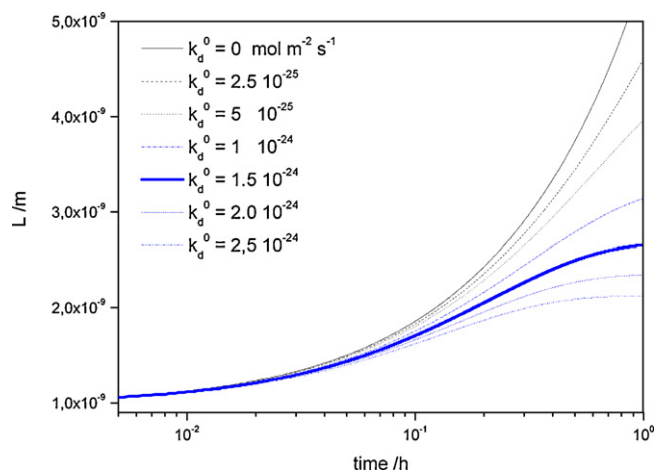


Fig. 33. Evolution of the oxide layer thickness  $L$  with time for  $V=0.0$  V/SHE and for different values of  $k_d^0$ .

thickness is shown in the inset of Fig. 34. Linear variation was obtained (7.45 nm/V). Such a variation is in qualitative agreement with those found in the literature. For instance, a similar variation has been obtained by Liu and Macdonald [58], even if the slope was 2 nm/V. An additional result concerning the evolution of the current density is presented in Fig. 35. In the investigated potential range, the current density decreased to the same value, i.e.  $1.7 \mu\text{A cm}^{-2}$ . This shows that for the parameter values listed in Table 2, the steady-state current density is potential independent. A specific result of DPCM is depicted in Fig. 36 which shows the variation of locations of the inner and the outer interfaces with time. At initial time, the location of the outer interface defines the origin of space. The initial location of the inner interface is defined by the initial thickness (1 nm). At short times, the outer interface moves toward the negative direction (in solution) and the inner interface moves toward the positive direction (in the metal). This is due to the effect of the Pilling–Bedworth ratio which is equal to 2.1. For longer times, both interfaces move toward the positive direction. The motion direction change of the outer interface results from the competition between the expansion due to the Pilling–Bedworth ratio and the rate of the *host lattice dissolution* reaction. It can also be seen on this figure that the dimensionless oxygen vacancies concentration is always low ( $<0.01$ ).

Unfortunately, the comparison between the predicted layer thickness given by DPCM and those available in the literature is at the moment only qualitative. Concerning the steady-state thick-

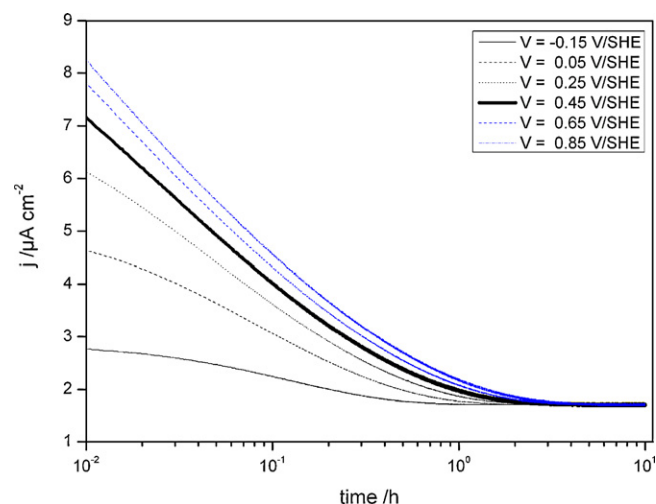


Fig. 35. Evolution of the current density  $j$  with time for different values of the applied potential  $V$ .

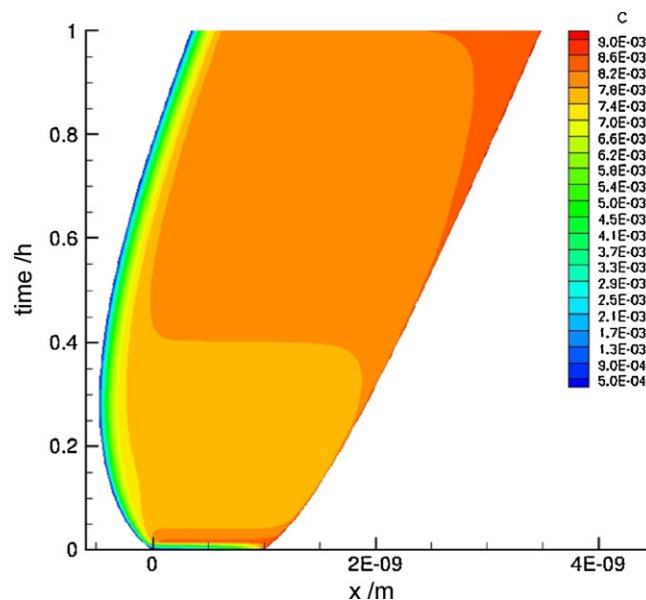


Fig. 36. Evolution of the location of the outer and inner interfaces with time for  $V=0.05$  V/SHE. The concentration of oxygen vacancies is indicated by the color on the right band. (For interpretation of the references to color in this figure legend, the reader is referred to the web version of the article.)

nesses, the values obtained thanks to DPCM are higher than those obtained in [58]. However, it must be outlined that the steady-state thicknesses evaluated by Liu and Macdonald [58] are lower than the instantaneous thicknesses measured by Szklarska-Smialowska and Kazlowski [57] after 1 h of polarization in the same experimental conditions ( $T=22$  °C,  $\text{pH}=8.4$ ). Moreover as mentioned above, no steady-state has been observed after 1 h of polarization. One could thus assume that if steady-state thickness was reached for longer times, it would be higher than those measured after 1 h. Concerning the current density, the decreases of current densities are narrower than those measured by Szklarska-Smialowska and Kazlowski [57], which extended over more than three decades for over 1 h of polarization.

## 6. Discussion

DPCM could be considered as an expansion of PDM or MCM. The solving of the Poisson equation takes the place of the homo-

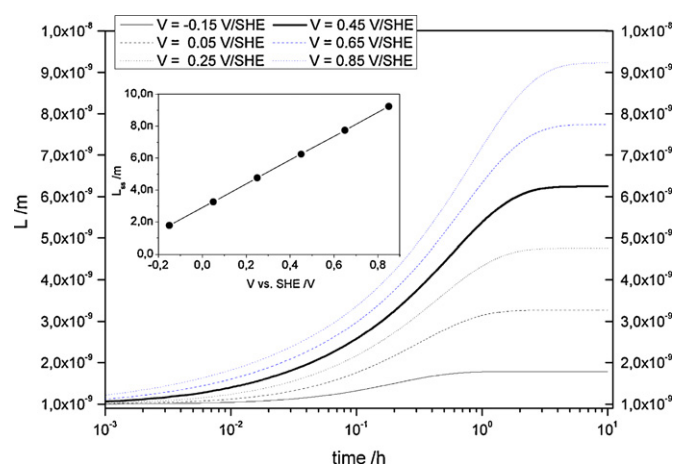
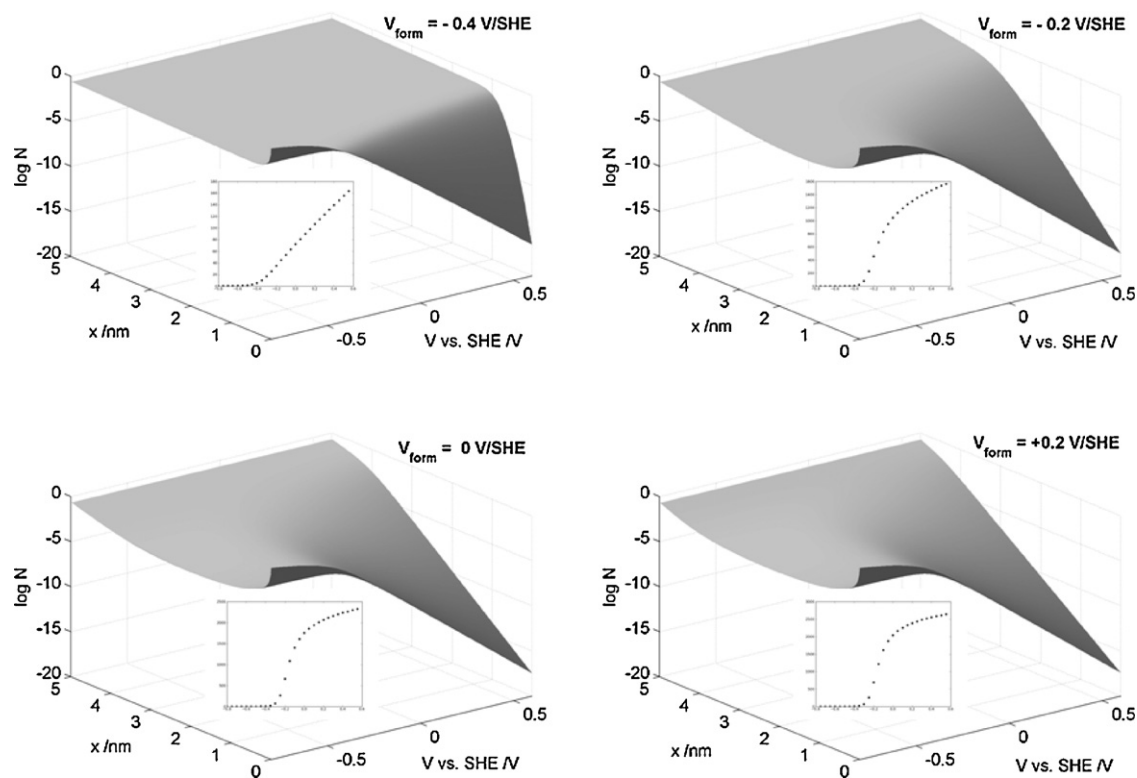


Fig. 34. Evolution of the oxide layer thickness  $L$  with time for different values of the applied potential  $V$ .



**Fig. 37.** Evolution of the electrons concentration profiles with the applied potential  $V$  in oxide layer formed at several  $V_{\text{form}}$  potentials for  $L = 5$  nm. Insets: the corresponding Mott–Schottky plot.

geneous mean field assumption. The linear relation (2) between the outer voltage and the applied potential  $V$  has been replaced by a description of the outer and inner interfaces based on the Helmholtz capacitance and the corresponding pzc voltage. Such a description allows calculating the charge carried by either the solution or the metal. The counterpart of this expansion is that DPCM has no analytical solution.

Another difference concerns the moving interfaces. The moving of the outer and the inner interfaces are considered in a fixed landmark whereas PDM and MCM consider only the variation of the layer thickness, i.e. the location of one interface (inner or outer) is calculated in a landmark linked to the other (outer or inner). The use of a fixed landmark in DPCM allows taking into account the Pilling–Bedworth ratio in a simple way.

The results presented in Section 4 have been obtained for a simplified system consisting mainly in a solution in contact with iron covered by a homogeneous iron spinel like oxide layer of fixed thickness. In this simplified situation, DPCM led to electrons concentration profiles consistent with the Mott–Schottky model. An accumulation layer was formed for applied potentials lower than the flat band potential and a depletion layer was formed for higher potentials. It has been shown that the flat band potential was linked to the potential of zero charge of interfaces. It has been shown in Section 4.2 that the Mott–Schottky model stood even if thermal equilibrium for electrons was not fulfilled. It has been also shown that the seeming donor density  $N_d$  was dependent on the octahedral iron concentration profile. When this profile was homogeneous, Mott–Schottky plots have been obtained. When this profile was not homogeneous, deviations from linearity on the Mott–Schottky plots have been observed (cf. Section 4.4). To explain these deviations, it is needed to have a global overview of changes for the electrons concentration profiles. This overview is presented in Fig. 37. For all oxide layers formed at different potentials  $V_{\text{form}}$ , each concentration profile exhibited an accumulation

layer in the cathodic range (outlined by the dashed circle) and a depletion layer in the anodic range. For each  $V_{\text{form}}$ , the corresponding shape of the Mott–Schottky plot is recalled in the inset. At  $V_{\text{form}} = -0.4$  V/SHE, the Mott–Schottky plot exhibited a large linear range for  $V > -0.4$  V/SHE (cf. Fig. 25). In this potential range, the electrons concentration profile showed depletion over a restricted thickness increasing up to 1 nm. Beyond, the concentration profile was homogeneous.

From  $V_{\text{form}} \geq -0.2$  V/SHE, deviation from linearity was observed on the Mott–Schottky plots (see the insets). This corresponded to a growth of the depletion layer which reached the size of the oxide layer. Beyond  $V_{\text{form}} \geq 0$  V/SHE, there was no more homogeneous range on the surface profile. Stimming has emphasized that there were two main reasons for deviation from linearity in Mott–Schottky plot [59]. One was the existence of multiple donor levels. The other was a varying concentration of donors. Fig. 37 illustrates the latter reason.

The growth of an accumulation or a depletion layer is of primary importance on the kind of iron cations released in the solution (ferrous or ferric). The oxidation of iron takes place at the inner interface (cf. Fig. 3). Octahedral ferric cations are injected into the oxide layer. At the outer interface, these octahedral ferric cations are released. In a potential range where depletion layer has grown, the electrons concentration at the outer interface  $c_e^0$  is low. From (21), the rate of reduction per ferric cation in solution would be low ( $k_r^0 c_e^0$ ). So, the iron cations would be released mainly as ferric cations. In a potential range where accumulation layer stands,  $c_e^0$  is high. The rate of reduction per ferric cations in solution would be high. Each ferric cation released by the *ferric release* step would be captured by the *ferrous release* step and reduced to ferrous cation. So, the iron cations would be released mainly as ferrous cations. The actual ratio between ferrous and ferric release would depend on the potential but also on the hydrodynamic features of the solution in the vicinity of the outer interface. If the flow rate is

high as in the case of a rotating disc electrode, some ferric cations would be drained off and not reduced. For stagnant solution, the ratio between ferrous and ferric release would depend only on the potential.

For all the calculations presented in this paper, the Mott–Schottky plots have been built in from the relation (30). This relation involves a term  $\alpha(V)$  which is the derivative of  $\Delta\phi_0$  vs. the applied potential  $V$ . This term  $\alpha(V)$  is equivalent to the outer interface polarizability  $\alpha_{fjs}$  introduced in the Point Defect Model and in the Mixed Conduction Model. Both models assume that  $\alpha_{fjs}$  is constant. The results obtained with DPCM are contradictory. For all the computations presented here,  $\alpha(V)$  was potential dependent (see Fig. 16). Moreover, a constant value for  $\alpha(V)$  could not give Mott–Schottky plots consistent with those published in the literature because  $C^{-2}$  would be also potential independent.

The main result of DPCM was that space charge layers could grow at the outer and the inner interfaces. This results from the charges carried by the solution and/or the iron. In our knowledge, DPCM is the only model to take into consideration these charges. The net electroneutrality is considered over the solution–oxide layer–metal system. The numerical model recently published by Vankerberghen [19] is quite similar to DPCM but does not take into account the charges carried either by the solution or by the metal. In the Vankerberghen's model, the electroneutrality is restricted to the oxide layer. The potential and the concentration profiles obtained with this model do not exhibit well pronounced space charge layers.

## 7. Conclusions

The Diffusion Poisson Coupled Model (DPCM) is proposed to describe the oxidation of iron in anaerobic neutral or slightly alkaline solution. These chemical conditions correspond to those expected for the geological repository of nuclear wastes in France. This model assumes that the solution is in contact with a dense disordered spinel like oxide layer which covers the iron. No analytical solution exists for this model. Its resolution must be numerical. This model consists in three modules: the electrostatic, the kinetics and the moving boundaries modules.

The electrostatic module gives the potential profile in the solution–oxide layer–metal system. It involves the Poisson equation and two boundary equations which are a combination of the Gauss law and the Helmholtz capacitance relation. The kinetics module gives the concentration profiles; one per each charge carrier. It involves the two Fick laws. The Nernst–Planck version of the first one is used. The two boundary equations needed to solve the second Fick law are obtained from the reaction path which is specific of the system under consideration. That for the case of iron covered by a disordered spinel iron oxide has been detailed here. The moving boundaries module gives the locations of the two interfaces which bound the oxide layer. It involves a solid state reaction which converts the metal into its oxide and a dissolution step. These three modules are coupled because each module involves the solution of the others.

Firstly, DPCM has been tested in a simplified situation where the locations of the outer (solution–oxide) and the inner (oxide–iron) interfaces are fixed. It has been shown that in this simplified situation, DPCM was in agreement with the Mott–Schottky model when the iron concentration profile was homogeneous. When the iron concentration profile was not homogeneous, deviation from Mott–Schottky model has been observed. Nevertheless in all cases considered in this paper, the electrons concentration profile exhibited an accumulation layer for applied potentials lower than the potential of zero charge of the outer interface and a depletion layer for higher potentials. It has been also shown that

deviation from the Mott–Schottky model came from the growth of the space charge layer to size higher than the oxide layer thickness.

The features of the outer interface have been described by a potential of zero charge and a constant Helmholtz capacitance. These features played a major role on the kinetics results. The reaction path proposed in this paper assumes that the oxidation of iron at the inner interface leads always to ferric cations injected in the oxide layer. Nevertheless, it has been shown that the ratio of the ferrous to ferric releases in solution was monitored by the electrons concentration profile. For applied potentials lower than the pzc of the outer interface, the iron cations were mainly released in solution as ferrous cations. For higher potentials, the iron cations were mainly released as ferric cations.

Finally, DPCM with moving boundaries has been tested. The expected results of the literature have been obtained, i.e. linear variation of the steady-state thickness with applied potential and a steady-state current density–potential independent.

## Acknowledgments

This work has been supported by the French power supplier EDF and by the Nuclear Waste Management Agency ANDRA.

## References

- [1] C.Y. Chao, L.F. Lin, D.D. Macdonald, *J. Electrochem. Soc.* 128 (1981) 1187.
- [2] L.F. Lin, C.Y. Chao, D.D. Macdonald, *J. Electrochem. Soc.* 128 (1981) 1194.
- [3] C.Y. Chao, L.F. Lin, D.D. Macdonald, *J. Electrochem. Soc.* 128 (1981) 1874.
- [4] D.D. Macdonald, M.U. Macdonald, *J. Electrochem. Soc.* 137 (1990) 2395.
- [5] D.D. Macdonald, S.I. Smedley, *Corros. Sci.* 31 (1990) 667.
- [6] D.D. Macdonald, S.I. Smedley, *Electrochim. Acta* 35 (1990) 1949.
- [7] D.D. Macdonald, S.R. Biaggio, H. Song, *J. Electrochem. Soc.* 139 (1992) 170.
- [8] D.D. Macdonald, *J. Electrochem. Soc.* 139 (1992) 3434.
- [9] L. Zhang, D.D. Macdonald, E. Sikora, J. Sikora, *J. Electrochem. Soc.* 145 (1998) 898.
- [10] L. Zhang, D.D. Macdonald, *Electrochim. Acta* 43 (1998) 679.
- [11] D.D. Macdonald, *Pure Appl. Chem.* 71 (1999) 951.
- [12] M. Bojinov, G. Fabricius, T. Laitinen, K. Makela, T. Saario, G. Sundholm, *Electrochim. Acta* 45 (2000) 2029.
- [13] M. Bojinov, T. Laitinen, K. Makela, T. Saario, *J. Electrochem. Soc.* 148 (2001) B243.
- [14] I. Betova, M. Bojinov, A. Englund, G. Fabricius, T. Laitinen, K. Makela, T. Saario, G. Sundholm, *Electrochim. Acta* 46 (2001) 3627.
- [15] B. Beverskog, M. Bojinov, A. Englund, P. Kinnunen, T. Laitinen, K. Makela, T. Saario, P. Sirkia, *Corros. Sci.* 44 (2002) 1901.
- [16] B. Beverskog, M. Bojinov, P. Kinnunen, T. Laitinen, K. Makela, T. Saario, *Corros. Sci.* 44 (2002) 1923.
- [17] C. Lukac, J.B. Lumsden, S. Smialowska, R.W. Staehle, *J. Electrochem. Soc.* 122 (1975) 1571.
- [18] M. Beuchler, P. Schmuki, H. Boehni, *J. Electrochem. Soc.* 144 (1997) 2307.
- [19] M. Vankerberghen, *Corros. Sci.* 48 (2006) 3609.
- [20] Y. Adda, J. Philibert, *La diffusion dans les solides Chapitre XVI: la diffusion en champ électrique*, vol. 2, INSTN, Saclay, 1966, p. 893.
- [21] A. Vinsot, J. Delay, *12th Water–Rock Interaction International Workshop*, Kunming, China, 2007, p. 663.
- [22] C. Beaucaire, H. Pitsh, P. Toulhoat, S. Motellier, D. Louvat, *Appl. Geochem.* 15 (2000) 667.
- [23] F. Walz, *J. Phys.: Condens. Matter* 14 (2002) R285.
- [24] D. Ihle, B. Lorenz, *J. Phys. C: Solid State Phys.* 18 (1985) L647.
- [25] M.I. Klinger, A.A. Samokhvalov, *Phys. Stat. Sol. B* 79 (1977) 9 (see p. 13).
- [26] S. Iida, K. Mizushima, M. Mizoguchi, J. Mada, S. Umemura, J. Yoshida, K. Nakao, *Journal de physique, Colloque* 38 (1977) C1.
- [27] J.M.D. Coey, A.H. Morrish, G.A. Sawatzky, *Journal de physique, Colloque* 32 (1971) C1.
- [28] R. Dieckmann, H. Schmalzried, *Ber. Bunsenges. Physik. Chem.* 81 (1977) 344.
- [29] R. Dieckmann, H. Schmalzried, *Ber. Bunsenges. Physik. Chem.* 81 (1977) 414.
- [30] R. Dieckmann, T.O. Mason, J.D. Hodge, H. Schmalzried, *Ber. Bunsenges. Physik. Chem.* 83 (1978) 778.
- [31] R. Dieckmann, *Ber. Bunsenges. Physik. Chem.* 86 (1982) 112.
- [32] R. Dieckmann, C.A. Witt, T.O. Mason, *Ber. Bunsenges. Physik. Chem.* 87 (1983) 495.
- [33] R. Dieckmann, H. Schmalzried, *Ber. Bunsenges. Physik. Chem.* 90 (1986) 564.
- [34] M. Backhaus-Ricoult, R. Dieckmann, *Ber. Bunsenges. Physik. Chem.* 90 (1986) 690.
- [35] A.J. Davenport, L.J. Oblonsky, M.P. Ryan, M.F. Toney, *J. Electrochem. Soc.* 147 (2000) 2162.

- [36] J.E. Parrott, Reformulation of boundary conditions at metal–semiconductor contacts, Metal–semiconductor contacts, Manchester, Conference Series N°22, 1974, p. 20.
- [37] V.L. Moruzzi, J.F. Janak, A.R. Williams, Calculated Electronic Properties of Metals, Pergamon Press Inc., New York, 1978, p. 84.
- [38] J. Friedel, in: J.M. Ziman (Ed.), The Physics of Metals, Cambridge University Press, London, 1969, p. 340.
- [39] F. Martin, C. Bataillon, M. Schlegel, *J. Nucl. Mater.* 379 (2008) 80.
- [40] C. Chanais-Hillairet, C. Bataillon, *Numer. Math.* 110 (2008) 1.
- [41] A.C. Makrides, *J. Electrochem. Soc.* 111 (1964) 392.
- [42] J. Chivot, Thermodynamique des produits de corrosion, diagramme E-pH en fonction de la temperature, Collection Sciences & Techniques, ANDRA 2004 ISBN 2-9510108-6-9, ISSN: 1629-7237.
- [43] A. Natarajan, G. Oskam, P.C. Searson, *J. Phys. Chem. B* 102 (1998) 7793.
- [44] E.C. Gaucher, P. Blanc, F. Bardot, G. Braibant, S. Buschaert, C. Crouzet, A. Gautier, J.P. Girard, E. Jacquot, A. Lassin, C. Negrel, C. Tournassat, A. Vinsot, S. Atlmann, *C. R. Geosci.* 338 (2006) 917.
- [45] P. Schmuki, M. Bucher, S. Virtanen, H. Bohni, R. Muller, L.J. Gauckler, *J. Electrochem. Soc.* 142 (1995) 3336.
- [46] M. Buchler, P. Schmuki, H. Bohni, *J. Electrochem. Soc.* 145 (1998) 378.
- [47] P.A. Castro, E.R. Vago, E.J. Calvo, *J. Chem. Soc., Faraday Trans.* 92 (1996) 3371.
- [48] E.R. Vago, E.J. Calvo, *J. Electroanal. Chem.* 339 (1991) 41.
- [49] E. Sikora, D.D. MacDonald, *J. Electrochem. Soc.* 147 (2000) 4087.
- [50] U. Stimming, J.W. Schultze, *Berichte Bunsen-Gesellschaft* 80 (1976) 1297.
- [51] A.M. Sukhotin, M.S. Grilikhes, E.V. Lisovaya, *Electrochim. Acta* 34 (1989) 109.
- [52] E.B. Castro, J.R. Vilche, *Electrochim. Acta* 38 (1993) 1567.
- [53] Y.F. Cheng, J.L. Luo, *Electrochim. Acta* 44 (1999) 2947.
- [54] H. Gerisher, *Electrochim. Acta* 35 (1990) 1677.
- [55] A.T. Fromhold, E.L. Cook, *Phys. Rev.* 163 (1967) 650.
- [56] M.S. Grilikhes, A.M. Sukhotin, Ya. Shik, *Sov. Electrochem.* 23 (1987) 1430.
- [57] Z. Szklarska-Smialowska, W. Kazlowski, *J. Electrochem. Soc.* 131 (1984) 234.
- [58] J. Liu, D. Macdonald, *J. Electrochem. Soc.* 148 (2001) B425.
- [59] M.H. Dean, U. Simming, *Corros. Sci.* 29 (1989) 199.
- [60] L. Garcell, M.P. Morales, M. Andres-Verges, P. Tartaj, C.J. Sema, *J. Colloid Interface Sci.* 205 (1998) 470.
- [61] R.E. Hummel, *Electronic Properties of Materials*, Springer-Verlag, 1985, p. 306, ISBN 3-540-15631-3 and ISBN 0-387-15631-3.